



Structural topology optimization considering both performance and manufacturability: strength, stiffness, and connectivity

Chao Wang^{1,2} · Bin Xu^{1,2} · Zunyi Duan^{1,2} · Jianhua Rong^{3,4}

Received: 9 July 2020 / Revised: 17 October 2020 / Accepted: 23 October 2020 / Published online: 13 January 2021
© Springer-Verlag GmbH Germany, part of Springer Nature 2021

Abstract

Structural topology optimization considering both performance and manufacturability is very attractive in engineering applications. This work proposes a formulation for structural topology optimization to achieve such a design, in which material strength, structural stiffness, and connectivity are simultaneously considered by integrating stress and simply-connected constraints into the compliance minimization problem. An effective solution algorithm consisting of different optimization techniques is introduced to handle various numerical difficulties resulted from this relatively complex multi-constraint and multi-field problem. Except for the stress penalization and aggregation techniques, the regional measure strategy is used together with the stability transformation method-based correction scheme to address stress constraints, which is also applied to the Poisson equation-based scalar field constraint in the simply-connected constraint. Numerical examples are presented to assess the features of the achieved design along with the performance of the employed algorithm. Comparisons with pure compliance, pure stress, and pure connectivity designs are provided to illustrate differences arising in the proposed design with respect to traditional approaches, also the necessity. Innovative manufacturing-oriented designs with consideration of the strength, stiffness, and connectivity are now available.

Keywords Design for manufacturing · Topology optimization · Stress constraints · Connectivity constraint · Aggregation technique

1 Introduction

Topology optimization, as a powerful tool for the conceptual design of structures, has attracted widespread attentions in academia and industry (Bendsøe and Sigmund 2003). Over the years, most efforts have been devoted to improving the design performance such as material strength, structural stiffness, and

stability. Recently, increasing attentions have been paid to the manufacturability of optimized designs from the perspective of manufacturing processes (Liu et al. 2018). Nevertheless, performance and manufacturability considerations are usually treated separately. Therefore, the combination of these two important and indispensable requirements in structural topology optimization would be a highly valuable but challenging task. This has motivated the present work to investigate such a formulation, in which the common requirements of material strength, structural stiffness, and connectivity (a critical manufacturing process constraint) are considered.

It is acknowledged that structural stiffness is one of the basic requirements for optimized designs in engineering. Thus, an overwhelming majority of previous works focus on minimizing the structural compliance (equivalents to maximizing the structural stiffness) with a prescribed material volume, i.e., the compliance minimization problem. For more detailed information on this field, readers can refer to Eschenauer and Olhoff 2001, Bendsøe and Sigmund 2003, and Rozvany 2009. Despite the mature of this formulation,

Responsible Editor: Jianbin Du

✉ Bin Xu
xubin@nwpu.edu.cn

- ¹ School of Mechanics, Civil Engineering & Architecture, Northwestern Polytechnical University, Xi'an 710072, China
- ² Institute of Structural Health Monitoring and Control, Northwestern Polytechnical University, Xi'an 710072, China
- ³ School of Automotive and Mechanical Engineering, Changsha University of Science and Technology, Changsha 410114, China
- ⁴ Key Laboratory of Safety Design and Reliability Technology for Engineering Vehicle, Changsha 410114, China

its extended application in the combination of the strength and connectivity is still an open problem.

Another fact is that designs considering stiffness alone are insufficient to cope with complex working conditions in practical engineering. The strength failure of material is sometimes even more important than the requirement of structural stiffness from the safety point of view (Duysinx et al. 2008). If material strength is not considered in the conceptual design of engineering structures, the obtained designs are susceptible to post-processing or even rework, resulting in unexpected costs. Consequently, researches have been done to formulate topology optimization settings considering stress (Duysinx and Bendsøe 1998). Some related works for practical engineering problems can also be found in (Luo and Kang 2012; Luo et al. 2017). However, there are few reports of stress problems involving complex manufacturing process constraints. On the other hand, handling stress issues in topology optimization itself is a challenging work, in which three main difficult problems generally need to be overcome: the stress singularity (mainly limited to density-based approaches with the existence of intermediate densities), the local nature of stress constraints, and the highly nonlinear stress behavior (Le et al. 2010). Effective stress techniques such as relaxation approaches (Cheng and Guo 1997; Duysinx and Bendsøe 1998; Bruggi and Venini 2008; Bruggi 2008; Le et al. 2010), aggregation techniques (Yang and Chen 1996; Duysinx and Sigmund 1998; Paris et al. 2009; Luo et al. 2013), regional measures (Paris et al. 2010; Le et al. 2010; Holmberg et al. 2013), and correction schemes (Le et al. 2010; Yang et al. 2018) have been proposed to overcome these challenges. Although these methods work well for general stress problems, their performance on manufacturable stress designs is not clear. For complex optimization conditions, the design usually presents unpredictable numerical responses during the optimization process, which would bring various challenges to the stress solution, thereby being a subject worthy of intensive research.

Admittedly, high-performance designs involving the stiffness and strength could be achieved with the above efforts, but the resulting sophisticated structures pose huge challenges to not only CAD modeling but also manufacturing (Gao et al. 2015; Liu and Ma 2016; Liu et al. 2018). Usually, complex features such as framework-like structures and enclosed voids are not directly manufacturable or even not manufacturable at all, due to incompatibility with the manufacturing process. As a result, the widespread application of topology optimization is limited to some degree. One solution is to modify the optimized design to a manufacturable one based on the judgment and experience of engineers. Extensive modifications, however, are inadvisable in terms of cost and performance impact. Therefore, a preferable method is to include manufacturability considerations in topology optimization directly (Liu and Ma 2016; Liu et al. 2018).

As one of the most important manufacturing process constraints, the simply-connected constraint to avoid enclosed voids (a typical connectivity requirement) is required in the structural design for both additive manufacturing (AM) and traditional manufacturing (TM) processes (Diegel et al. 2010; Gao et al. 2015; Liu and Ma 2016). In the AM process such as selective laser sintering (Kruth et al. 2005) and fused deposition modeling (Hutmacher et al. 2001; Zein et al. 2002), enclosed void configurations make the removal of support materials difficult and uneconomic. For the TM process such as casting, milling, and turning, the preparation of enclosed voids is even impractical (Liu and Ma 2016). There have been a few reports specifically on the suppression of enclosed voids in topology optimization. Considering the AM process, Zhou and Zhang (2019) extended the feature-driven topology optimization method (Zhang et al. 2017a, b) to eliminate enclosed voids. Liu et al. (2015) constructed an auxiliary steady-state heat transfer model to detect and suppress enclosed voids. Other related methods were mainly developed for certain TM processes (Zhou et al. 2002; Xia et al. 2010; Gersborg and Andreasen 2011; Vatanabe et al. 2016; Li et al. 2018; Qian 2017; Wang and Kang 2017; Langelaar 2019), where enclosed voids are always tightly coupled with other special manufacturing considerations such as undercuts and symmetry, thus leading to over conservative solutions for some enclosed void problems. In the process of seeking design manufacturability, these methods fully consider the effect of manufacturability on structural stiffness and/or material volume; however, none of them takes the effect on material strength into account. In fact, numerical results here clearly show that the introduction of manufacturability considerations, or at least the simply-connected constraint, has a significant impact on the strength.

Surely the three practical requirements of strength, stiffness, and connectivity in structural topology optimization have already been considered separately or in groups. To the authors' best knowledge, however, no work integrates them all into a unified formulation, to achieve manufacturable designs with high performance. Besides, the combination of complex stress and connectivity constraints involves interaction issues, which challenge the existing constraint measures, whether in stress constraints or connectivity constraints. Hence, the development of effective solution algorithms is also very necessary.

In view of the above-mentioned facts, this work aims to propose such a unified formulation, which takes the strength, stiffness, and connectivity into account in structural topology optimization. The formulation is an extension of the traditional compliance minimization. The novelty of this proposal comes from the inclusion of stress and simply-connected constraints concurrently. Also, an effective solution algorithm combining different optimization techniques is developed to

overcome various numerical difficulties involved in the solution for this special formulation.

The rest of this work is organized as follows. In Section 2, the proposed topology optimization problem formulation is presented. The detailed schemes for the stress and simply-connected constraints are discussed in Sections 3 and 4, respectively. In Section 5, the sensitivity analysis and optimization process are put forward. Test examples are presented in Section 6. And, concluding remarks are finally drawn in Section 7.

2 Problem formulation

In this research, the classical density approach (Sigmund and Maute 2013) is adopted for the topology optimization framework. The structural problem with linear, elastic, and isotropic domain under static loads is considered and solved through the displacement-based finite element method (FEM) (Bathe 1996). Each finite element i is assigned a (relative) density x_i varying from 0 (i.e., void) to 1 (i.e., solid), which corresponds to a physical density \bar{x}_i that determines the physical properties associated with the element i . Physical densities $\bar{\mathbf{x}}$ are associated with element densities \mathbf{x} (i.e., the design variables) through density filtering (Bruns and Tortorelli 2001; Bourdin 2001) and threshold projection (Wang et al. 2011).

To simultaneously consider the strength, stiffness, and connectivity in structural topology optimization, the well-known topology optimization formulation for minimum compliance is expanded to integrate both stress and simply-connected constraints. And, the commonly used von Mises failure stress criterion is followed. Next subsections aim to present the optimization problem (Section 2.1) and the density filter-based threshold projection scheme (Section 2.2).

2.1 Optimization problem

After considering the stress and simply-connected constraints, we have the minimum compliance formulation with volume, stress, and connectivity constraints (MCVSC) as

$$\begin{aligned}
 & \text{Find : } \mathbf{x} = [x_1, x_2, \dots, x_i, \dots, x_N]^T \\
 & \text{Min : } C(\bar{\mathbf{x}}) \mathbf{F}^T \mathbf{U} \\
 & \text{Subject to :} \\
 & \text{In the elastic} \\
 & \text{mechanics field} \left\{ \begin{aligned} & \mathbf{K}\mathbf{U} = \mathbf{F} \\ & V(\bar{\mathbf{x}}) \leq f \cdot V_0 (\text{Volume constraint}) \\ & \sigma_i^{vM}(\bar{\mathbf{x}}) \leq \bar{\sigma} (\text{Stress constraints}) \end{aligned} \right. \quad (1) \\
 & \text{In the} \\
 & \text{electrostatic field} \left\{ \begin{aligned} & \mathbf{K}^\phi \mathbf{U}^\phi = \mathbf{F}^\phi \\ & \phi_{EPC} \leq 0 (\text{Simply-connected constraint}) \\ & 0 \leq x_i \leq 1 \end{aligned} \right.
 \end{aligned}$$

where \mathbf{x} is the vector of design variables x_i (i.e. the element densities), N is the number of elements used to discretize the design domain, C is the structural compliance, \mathbf{F} and \mathbf{U} are the global force and displacement vectors, respectively, and \mathbf{K} is the global stiffness matrix, $V(\bar{\mathbf{x}}) = \sum_{i=1}^N \bar{x}_i v_i$ is the total material volume, v_i is the volume of element i , f is the prescribed material volume fraction, V_0 is the design domain volume, σ_i^{vM} is the von Mises equivalent stress of element i , to be defined in Section 3, $\bar{\sigma}$ is the allowable stress limit, \mathbf{K}^ϕ is the global dielectric matrix, \mathbf{U}^ϕ and \mathbf{F}^ϕ are the global nodal potential and electrostatic load vectors, respectively, and ϕ_{EPC} is an Electrostatic Potential Constraint (EPC) related to the structural connectivity detailed in Section 4. With the modified Solid Isotropic Material with Penalization (SIMP) method (Sigmund 2007), the local stiffness matrix of element i becomes $\mathbf{k}_i(\bar{x}_i) = [E_{\min} + (\bar{x}_i)^p (E_0 - E_{\min})] \mathbf{k}_{0,i}$, where E_0 is the Young's modulus of the solid material, $E_{\min} = 10^{-9} E_0$ is the Young's modulus of the void material (to avoid singularity of the stiffness matrix), p is the penalization power (typically chosen as $p = 3$, and also in this research), and $\mathbf{k}_{0,i}$ is the element stiffness matrix for unit Young's modulus.

For comparison, the other three optimization problems related to the MCVSC problem are also discussed in this work. These problems have the same objective function but different constraints, as listed in Table 1. Among them, the MCVSC problem will be primarily investigated.

2.2 Density filter-based threshold projection

It is recognized that implementing the density-based topology optimization with the physical densities set equal to the design variables will lead to numerical problems with checkerboard patterns and mesh-dependence (Sigmund and Petersson 1998). Hence, some restrictions on the above four optimization problems must be imposed. A common method is to filter sensitivities or densities. Both sensitivity filter (Sigmund 1997) and density filter (Bruns and Tortorelli 2001; Bourdin 2001) perform well for the standard MCV problem. For the relatively complex MCVS problem involving stress constraints, however, the consistent density filter is preferable (Le et al. 2010). Furthermore, numerical experiences show that the density filter is also beneficial for addressing the ill-posed problem of the MCV problem (Wang et al. 2020a). Therefore, only the density filter is considered in this study to meet the rigorous numerical challenges from the complex MCVSC problem.

Using the linear density filter, the filtered density variables \hat{x}_i is given by

$$\hat{x}_i = \frac{\sum_{k \in NE_i} (H_{ik} v_k x_k)}{\sum_{k \in NE_i} (H_{ik} v_k)} \quad (2)$$

Table 1 Four different optimization problems

Minimum problem (M)	Objective function	Constraint function		
		Compliance (C)	Volume (V)	Stress (S)
MCV	√	√		
MCVS	√	√	√	
MCVC	√	√		√
MCVSC	√	√	√	√

Note: “√” denotes the selected term

where NE_i is the set of neighborhood elements x_k within the filter radius r_{\min} from the center of element x_i , the weight factor $H_{ik} = \max(0, r_{\min} - \Delta(i,k))$, and $\Delta(i,k)$ is the center-to-center distance between elements x_i and x_k .

Applying filtering techniques will cause gray transition areas with intermediate densities between void and solid phases, but this problem can be alleviated by using various projection techniques (Guest et al. 2004; Sigmund 2007; Xu et al. 2010; Wang et al. 2011). In this work, the effective threshold projection technique (Wang et al. 2011) is employed. All the filtered density values below a threshold x_0 are projected to 0 and the values above to 1. The projected physical density is computed by a projection function, which is controlled through a projection parameter β and expressed as

$$\left(\overline{\hat{x}}_i\right) = \frac{\tanh(\beta x_0) + \tanh\left[\beta\left(\hat{x}_i - x_0\right)\right]}{\tanh(\beta x_0) + \tanh[\beta(1 - x_0)]} \quad (3)$$

The threshold $x_0 \in [0, 1]$ regulates the inflection point of the projection function, determining the number of projected densities transformed to either 0 or 1, for $\beta \rightarrow \infty$. For $x_0 = 0$, the projection function coincides with the Heaviside step filter (Guest et al. 2004). For $x_0 = 1$, the projection function is consistent with the modified Heaviside step filter (Sigmund 2007). Here, the threshold is $x_0 = 0.5$, which several researches have proven to work well.

The parameter β determines the slope of the projection function. For $\beta \rightarrow 0$ we recover a linear behavior between filtered and physical densities, whereas for $\beta \rightarrow \infty$ we recover a Heaviside step function (Wang et al. 2011). Generally, a continuation strategy for β is employed to approach the step function gradually during the optimization process, starting from a small value up to a maximum value specified by the designer. The maximum value is usually chosen large enough to obtain crisp black and white designs (Wang et al. 2011), but this will cause the algorithm converges slowly, besides the appearance of the oscillation and instability of the iteration when β value changes.

To eliminate the continuation strategy, Guest et al. (2011) proposed simple modifications to the optimization algorithms and/or the Heaviside formulation, allowing the algorithms to start with large β values directly. Although the modifications are effective for traditional compliance and compliant inverter problems, they do not take the relatively complex problems with stress and/or connectivity into account. In fact, Da Silva et al. (2019a) have demonstrated that the parameter β has an important influence on the accuracy of stress evaluation at jagged edges and the proper choice of β is necessary for stress constrained problems. Le et al. (2010) also pointed out that prematurely generating black and white designs with jagged edges in iterations may not be preferable for stress problems. Recently, several works (da Silva et al. 2019a, b; Gao et al. 2020) have shown that the β continuation strategy with a moderate value for the maximum β is more suitable for the optimization problems with stress constraints. Therefore, we choose to gradually increase the value of β to a moderate and empirical maximum value through a continuation procedure during the optimization process in this study.

For a fair comparison, we carry out the same procedure for β tuning to solve the four optimization problems mentioned earlier, where the parameter β is set to be 1 within the initial 10 iterations, after that it is increased by 1 every 1 continuation steps until reaching a maximum value of 20. This procedure slows down the convergence but allows the optimization algorithm to effectively control the stresses and/or the connectivity, resulting in relatively good designs. Surely the parameters in this procedure could be further tuned for the specifically presented problems here. However, this is beyond the scope of this work.

3 Stress constraints

It is acknowledged that the solution of stress-constrained problems is non-trivial and still a standard challenge, being a topic worthy of further study. In this research, an effective stress constraint scheme combining different optimization

techniques is introduced to deal with stress-related numerical difficulties. The stress penalization strategy (Le et al. 2010) is utilized to address the singularity issue (Section 3.1). As regards the local nature of stress, the normalized P-norm stress measure is considered (Section 3.2), which is combined with the Stability Transformation Method (STM)-based correction scheme (Yang et al. 2018) to decrease the aggregation approximation error and stabilize the convergence process (Section 3.3). Given the poor local stress control of the global P-norm stress constraint, the block aggregated constraint approach (Paris et al. 2010) is employed to enhance the local stress control (Section 3.4). As for the highly nonlinear behavior, the consistent density filter-based threshold projection scheme (Section 2) is applied to the optimization problem statement and its solution algorithm, following (da Silva et al. 2019a, b; Gao et al. 2020). In this case, the constraint sensitivity information is numerically consistent with the optimization problem formulation, so that the convergence of the nonlinear programming algorithm is not excessively sacrificed (Le et al. 2010).

3.1 Stress penalization

The stress singularity stems from the discontinuity of the stress constraints at zero density, that is, elements can exhibit nonzero value and even high-stress value when the elemental densities decrease to zero, resulting in the non-removal of such elements (CHENG and JIANG 1992; Duysinx and Sigmund 1998). To circumvent this difficulty, some effective remedy schemes, such as the epsilon relaxation (Cheng and Guo 1997; Duysinx and Bendsøe 1998), the qp-relaxation approach (Bruggi and Venini 2008; Bruggi 2008), and the stress penalization strategy (Le et al. 2010), have been proposed to relax stress constraints, making the element stress and density can be reduced simultaneously. Besides, implementing topology optimization approaches without intermediate densities (e.g., the level set method and evolutionary method (Xie and Steven 1993)) can also avoid the singularity (Liang et al. 1999; Guo et al. 2011).

In this research, the commonly used stress penalization strategy (Le et al. 2010), which adopts a separate stress interpolation to further penalize the intermediate densities, is followed. Without loss of generality, the elemental centroid is selected as the only stress evaluation point for each element. Then, the penalized element stress vector becomes:

$$\boldsymbol{\sigma}_i = \left(\bar{\hat{x}}_i\right)^q \mathbf{D}_0 \mathbf{B}_i^c \mathbf{u}_i \quad (4)$$

where \mathbf{D}_0 is the constitutive elasticity tensor of the solid material, \mathbf{B}_i^c is the strain-displacement matrix at the element centroid, \mathbf{u}_i is the elemental displacement vector, and the prescribed penalization factor q is set to be 0.5 as suggested in (Le et al. 2010). The von Mises equivalent stress of element i reads:

$$\sigma_i^{vM} = \sqrt{\boldsymbol{\sigma}_i^T \mathbf{V} \boldsymbol{\sigma}_i} \quad (5)$$

For a plane stress state, the constant matrix \mathbf{V} is defined as:

$$\mathbf{V} = \begin{bmatrix} 1 & -1/2 & 0 \\ -1/2 & 1 & 0 \\ 0 & 0 & 3 \end{bmatrix} \quad (6)$$

corresponds to the following form

$$\sigma_i^{vM} = \left(\sigma_{i,x}^2 + \sigma_{i,y}^2 - \sigma_{i,x}\sigma_{i,y} + 3\sigma_{i,xy}^2\right)^{\frac{1}{2}} \quad (7)$$

in which $\sigma_{i,x}$, $\sigma_{i,y}$, and $\sigma_{i,xy}$ constitute the stress vector $\boldsymbol{\sigma}_i$.

Note that the above stress model is a physically inconsistent scheme for intermediate densities. This choice would simplify the computational effort for solving stress-constrained topology optimization problems, but also lead to the artificial removal of materials (Duysinx and Bendsøe 1998). Nonetheless, the threshold projection technique employed here can effectively remove intermediate densities, thereby significantly alleviating this physical inconsistency in the optimized design, as demonstrated in the works of (De Leon et al. 2015; Gao et al. 2020).

3.2 Normalized stress aggregation

The local nature of stress is another important issue for stress-constrained topology optimization problems. Ideally, stress constraints should be considered at every material point in the design domain. Even for finite element-based design problems with only one stress evaluation point per element, however, the number of stress constraints is still very large for practical applications due to the concomitant huge computational burden. To this end, some efficient techniques have been developed to improve the computational efficiency, such as the active set strategy-based local approaches (Duysinx and Bendsøe 1998; Bruggi and Duysinx 2012), the aggregation function-based techniques (Duysinx and Sigmund 1998; Le et al. 2010; Holmberg et al. 2013), and the augmented Lagrangian method (Pereira et al. 2004; Fancello 2006). In this study, the efficient aggregation techniques are adopted, which control the stress level by regulating the trend of the maximum stress σ_{\max} of the design domain. For this purpose,

both the P-norm (Duysinx and Sigmund 1998) and Kreisseimeier-Steinhauser (KS) (París et al. 2009) functions are available. Without loss of generality, we choose the traditional P-norm stress measure, which gives an approximation of the σ_{\max} and produces the P-norm stress constraint as follows:

$$\widehat{\sigma}^{PN} = \left[\sum_{i=1}^N (\sigma_i^{VM})^{ps} \right]^{\frac{1}{ps}} \leq \bar{\sigma} \tag{8}$$

where ps is the stress aggregation parameter. For $ps \rightarrow 1$, the P-norm function exhibits excessive smoothness and generates the average stress, whereas for $ps \rightarrow \infty$, the P-norm presents poor smoothness and approaches the σ_{\max} . Although a higher value of ps can provide a more accurate approximation to the σ_{\max} , the problem would also become ill-conditioned when ps increases, resulting in an oscillating behavior and even a failure of the optimization procedure (Duysinx and Sigmund 1998). A good choice for ps is based on a trade-off between the adequate smoothness and the accurate approximation (Le et al. 2010).

On the other hand, depending on the value of the stress constraint and the aggregation parameter, numerical accuracy problems can occur since $(\sigma_i^{VM})^{ps}$ in Eq. (8) will become very large (Holmberg et al. 2013). One solution is to normalize the P-norm measure with the stress limit, which gives a mathematically equivalent formulation as

$$\sigma^{PN} = \left[\sum_{i=1}^N \left(\frac{\sigma_i^{VM}}{\bar{\sigma}} \right)^{ps} \right]^{\frac{1}{ps}} \leq 1 \tag{9}$$

3.3 Correction of aggregated stress constraint

As discussed earlier, it is impractical to set the aggregation parameter to be a sufficiently large value. When this parameter takes a moderate value, however, there will inevitably be an approximation error between the approximate value and the actual value for the aggregation technique-based stress measure (Duysinx and Sigmund 1998; Verbart et al. 2017). In this case, depending on the magnitude of the approximate error, the actual stress level of the optimized design may deviate from the required stress limit to varying degrees. Therefore, it is not accurate enough to control the stress level of the obtained design just by the original P-norm stress measure (Le et al. 2010). To remedy this deficiency, Le et al. (2010) proposed an adaptive normalization scheme to better approximate the maximum stress. Recently, Yang et al. (2018) also presented the

STM-based stress correction scheme to achieve relatively accurate control of the stress level. By the STM-based correction scheme, one can obtain the corrected P-norm stress constraint as

$$\bar{\sigma}^{PN} = \sigma^s \cdot \sigma^{PN} - 1 \leq 0 \tag{10}$$

where c^s is the correction parameter, which is updated at every iteration during the optimization process by:

$$c_n^s = q_n^s \left[\frac{\max(\sigma_i^{VM})_n}{(\bar{\sigma} \cdot \sigma_n^{PN})} \right] + (1 - q_n^s) c_{n-1}^s \tag{11}$$

where c_n^s and q_n^s are the correction parameter and control factor in the n th iteration, respectively. In this work, $q^s = 0.5$ and $c_0^s = 1$ as suggested in (Yang et al. 2018).

3.4 Regional stress constraints

Although the corrected stress constraint, Eq. (10), would be effective for general stress problems, it still cannot avoid the poor control of the local stress state, especially for the relatively complex MCVSC problem here, because there is only a single global control over the entire design domain (Duysinx and Sigmund 1998; Le et al. 2010). To enhance the local stress control, París et al. (2010) first proposed an effective block aggregated constraints approach, which groups the elements of the design domain into several blocks, and imposes a single aggregated stress constraint for each block. Then, Le et al. (2010) and Holmberg et al. (2013) expanded the regional definitions. In this work, we propose to combine the above STM-based stress correction scheme with the block approach to strengthen the stress constraint. So, the corrected P-norm stress constraint for the region r is given by

$$\bar{\sigma}_r^{PN} = c_r^s \cdot \sigma_r^{PN} - 1 \leq 0, r = 1, 2, \dots, R \tag{12}$$

where c_r^s is computed independently for each region using Eq. (11) and σ_r^{PN} is calculated from Eq. (9) by only considering the elements grouped into the region r . For a better region definition, the interlacing approach suggested in (Le et al. 2010; Holmberg et al. 2013) is considered. Elements are sorted in descending order according to their stress level at the current iteration: $\{x_1, x_2, \dots, x_N: \sigma_1 \leq \sigma_2 \leq \dots \leq \sigma_N\}$ and then define the R regions as

$$\Omega_r \equiv \{x_r, x_{R+r}, x_{2R+r}, \dots\} \tag{13}$$

where Ω_r is the set of elements grouped into the region r . If the optimizer works perfectly, the design will improve as R

increases. Numerical experiments, however, demonstrated that the optimizer may converge to an inferior local optimum for a large value of R (Le et al. 2010). Hence, a moderate R value is preferred in practice. A more detailed discussion on the property of regional measures can be found in (Le et al. 2010; Holmberg et al. 2013).

4 Simply-connected constraint

In this work, the virtual temperature method proposed by Liu et al. (2015) for the simply-connected constraint is followed. Mathematically, it is a method of Poisson equation-based scalar field constraint (Li et al. 2016). The presentation of the Poisson method, however, cannot be inseparable from specific physical principles (Liu et al. 2015; Li et al. 2016). To this end, as a meaningful supplement for the Poisson method, the electrostatic model suggested in (Wang et al. 2020a) is used here instead of the temperature model (See Section 4.1). The expression of the electrostatic model is the same as that of the temperature model in mathematics. The motivation for using the electrostatic model is twofold.

On the one hand, the electrostatic model can also reasonably characterize the enclosed voids, while different physical fields have different physical laws, which can be used to inspire readers to further develop the Poisson method. On the other hand, the electrostatic theory will be beneficial to decipher the key constraint relation and the constraint boundary dependence hidden in the Poisson method. It would be helpful for readers to understand the Poisson method (Wang et al. 2020a).

Next, the corresponding material penalization scheme for topology optimization is presented in Section 4.2. In addition, considering the computational complexity of the scalar field constraints in the Poisson method and their similarity with stress constraints, we propose to introduce the related stress techniques described in Sections 3.2 to 3.4 to address the various numerical challenges that arise (see Section 4.3).

4.1 Electrostatic constraint model

In the electrostatic model, void materials are assumed to be positively charged carriers with strong dielectric capability, while solid materials are defined as the insulating media with poor dielectric capability, using the following material projection model:

$$\begin{cases} \varepsilon = \varepsilon^\phi, \rho = \rho^\phi, \text{for } x_i = 0 \\ \varepsilon = \mu \cdot \varepsilon^\phi, \rho = 0, \text{for } x_i = 1 \end{cases} \quad (14)$$

where ε and ρ are the material permittivity and electric charge density, respectively, ε^ϕ and ρ^ϕ are constants, and μ is a small positive value to prevent singularity. Especially, the user-specified domain boundary is grounded as a zero-potential reference, i.e., the EPC boundary Γ_{EPC} .

According to the electrostatics theory, a strong electrostatic field, quantified by the electric scalar potential ϕ , can be excited by the charged enclosed voids. Once the enclosed voids, however, are connected to the grounded boundary, a sharp potential decrease could happen. Then, by examining the maximum potential strength ϕ_{\max} of the structural electrostatic field, one can judge whether the structure contains enclosed voids. Thus, similar to the temperature method (Liu et al. 2015), the simply-connected constraint for avoiding enclosed voids in topology optimization can be equivalent to restricting the ϕ_{\max} , i.e., the electrostatic potential constraint ϕ_{EPC} as follows:

$$\phi_{\max} \leq \eta \cdot \phi_0 \quad (15)$$

where $(\eta \phi_0)$ is the constraint threshold for evaluating whether a structure contains enclosed voids; ϕ_0 is a basic reference threshold predefined by the user, which is usually calculated by considering all materials of the structure as void materials (Li et al. 2016); $\eta > 0$ is a constraint factor to correct the constraint threshold, which needs to be tuned for different problems to control the effectiveness of the EPC (Wang et al. 2020a). The second-order differential equation governing ϕ is the famous Poisson equation (Jin 2014):

$$-\nabla \cdot (\varepsilon \nabla \phi) = \rho \quad (16)$$

where ∇ is the differential symbol. For the above electrostatic problem, the specific boundary conditions are as follows:

$$\begin{cases} \phi = 0 & \text{on } \Gamma_D \\ (\varepsilon \nabla \phi) \cdot \mathbf{n} = 0 & \text{on } \Gamma_N \end{cases} \quad (17)$$

where Γ_D and Γ_N denote the Dirichlet boundary and the Neumann boundary, respectively, and \mathbf{n} is the outward normal unit vector of the boundary.

Note that, in the electrostatic model for simply-connected design, each EPC boundary Γ_{EPC} means a basic reference for evaluating the topological connectivity of the design, which is able to control the orientation of material distribution, that is, relying on the boundary to “drive away” solid materials and “adsorb” void materials. Different combinations of EPC boundaries constitute various EPC boundary conditions, corresponding to different optimization problems. As a result, the electrostatic model-based simply-connected design has an inherent EPC boundary condition dependence, that is, different EPC boundary conditions will lead to different optimized results (Wang et al. 2020a).

4.2 Material penalization

For the above electrostatic model, a modified SIMP-like material penalization is introduced to handle the related discretized problem in topology optimization. Then, the elemental material properties can be redefined based on Eq. (14) as

$$\begin{cases} \varepsilon_i^\phi(\widehat{x}_i) = \varepsilon_s^\phi + (1 - \widehat{x}_i)^{pe} (\varepsilon_v^\phi - \varepsilon_s^\phi) \\ \rho_i^\phi(\widehat{x}_i) = (1 - \widehat{x}_i) \rho_v^\phi \end{cases} \quad (18)$$

where ε_s^ϕ and ε_v^ϕ are the permittivities of the solid and void materials, respectively; $pe > 1$ is the penalization factor (the usually used value $pe = 3$ is followed here); and ρ_v^ϕ is the charge density of the void material. In this study, these material properties are given as $\varepsilon_v^\phi = 1$, $\varepsilon_s^\phi = 10^{-3}$, and $\rho_v^\phi = 1$, following (Wang et al. 2020a, b). Further parameter tuning may be beneficial, but this is not the focus of this research. Note that Eq. (18) is just one of the effective equivalent substitutions to Eq. (14). Accordingly, the element dielectric matrix \mathbf{k}_i^ϕ and the vector of element electrostatic load \mathbf{F}_i^ϕ read

$$\begin{cases} \mathbf{k}_i^\phi(\widehat{x}_i) = \varepsilon_i^\phi(\widehat{x}_i) \mathbf{k}_{0,i}^\phi \\ \mathbf{F}_i^\phi(\widehat{x}_i) = \rho_i^\phi(\widehat{x}_i) \mathbf{F}_{0,i}^\phi \end{cases} \quad (19)$$

where $\mathbf{k}_{0,i}^\phi$ is the element dielectric matrix for unit permittivity, and $\mathbf{F}_{0,i}^\phi$ is the element load vector for unit static charge density.

4.3 Effective constraint scheme

One can verify that the potential is indeed a local quantity similar to the stress, except that the potential is for nodes. Moreover, the potential is highly nonlinearly dependent on the design. Therefore, although the stress and potential constraints are different, their numerical difficulties in terms of the local nature and high nonlinearity are similar. Thus, some relevant stress measures may also be effective for the potential constraint. As a result, we propose to introduce the normalization, aggregation, correction, and regional measure techniques originally developed for stress constraints to overcome the numerical difficulties of the potential constraint.

(1) Normalized potential aggregation

Using the maximum function, the ϕ_{\max} in Eq. (15) can be expressed as

$$\phi_{\max} = \max_{j=1 \dots ND} (\varphi_j) \leq \eta \cdot \phi_0 \quad (20)$$

where φ_j is the nodal potential in the electrostatic model and ND is the total nodal number in the discrete design domain. The maximum function, however, is non-differentiable, which does not apply to the gradient-based algorithm. To ensure the differentiability of the constraint function in Eq. (15), the ϕ_{\max} can be stated by an aggregation function such as the P-norm function or the KS function. On the other hand, in the Poisson method, a larger scalar magnitude is helpful to distinguish different designs. Given the numerical accuracy problems resulted from the large values of constraint and aggregation parameter in the aggregation technique, it would be helpful to normalize the aggregated results. Consequently, without loss of generality, we give the normalized P-norm potential constraint as follows:

$$\phi^{PN} = \left\{ \sum_{j=1}^{ND} \left[\frac{\varphi_j}{(\eta \cdot \phi_0)} \right]^{pc} \right\}^{\frac{1}{pc}} \leq 1 \quad (21)$$

where pc is the potential aggregation parameter.

(2) Correction of aggregated potential constraint

Similar to the correction of the aggregated stress constraint described in Section 3.3, we introduce the STM-based correction scheme (Yang et al. 2018) to better approximate the maximum potential strength ϕ_{\max} . Then, the corrected P-norm potential constraint becomes:

$$\overline{\phi}^{PN} = c^c \cdot \phi^{PN} - 1 \leq 0 \quad (22)$$

where c^c is the correction parameter and updated at every iteration by

$$c_n^c = q_n^c \left[\frac{\max(\varphi_j)_n}{(\eta \cdot \phi_0) \cdot \phi_n^{PN}} \right] + (1 - q_n^c) c_{n-1}^c \quad (23)$$

where c_n^c and q_n^c are the correction parameter and the control factor in the n th iteration, respectively. $q^c = 0.5$ is set as a constant value and $c_0^c = 1$ is used here.

(3) Regional potential measure

To enhance the local control over the nodal potentials, the block aggregated constraint approach is also applied to the potential constraint. Here we group the nodes of the design domain into several regions and impose an aggregated potential constraint on each region. Accordingly, the corrected P-norm potential constraint for region t is formulated as

$$\overline{\phi}_t^{PN} = c_t^c \cdot \phi_t^{PN} - 1 \leq 0, t = 1, 2, \dots, Q \quad (24)$$

where c_t^c is calculated independently for each region using Eq. (23) and ϕ_t^{PN} is calculated from Eq. (21) by only considering the nodes in region t . To better define these regions, nodes d are sorted in descending order according to their potential level at the current iteration: $\{d_1, d_2, \dots, d_{ND}: \varphi_1 \leq \varphi_2 \leq \dots \leq \varphi_{ND}\}$ and the Q regions are defined as

$$\Omega_t \equiv \{d_t, d_{Q+t}, d_{2Q+t}, \dots\} \tag{25}$$

where Ω_t is the set of nodes grouped into the region t . Numerical experiences show that moderate Q -value is preferred in practice. As regards the high nonlinearity, the consistent density filter-based projection technique described in Section 2.2 is followed.

5 Solution aspects

5.1 Sensitivity analysis

In this study, the optimization problems listed in Table 1 are solved by the reasonable gradient-based Method of Moving Asymptotes (MMA) numerical optimizer (Svanberg 1987). The first-order sensitivity of the objective and constraints is then required by the optimizer to update the design variables.

Using the chain rule, the sensitivity of any function ψ with respect to the design variables x_e can be obtained by

$$\frac{\partial \Psi}{\partial x_e} = \sum_{i \in NE_e} \frac{\partial \Psi}{\partial \hat{x}_i} \frac{\partial \hat{x}_i}{\partial x_e} \tag{26}$$

where $\partial \hat{x}_i / \partial x_e$ is computed from Eq. (3) as

$$\frac{\partial \hat{x}_i}{\partial x_e} = \frac{\beta - \beta \left\{ \tanh^2 \left[\beta (\hat{x}_i - x_0) \right] \right\}}{\tanh(\beta x_0) + \tanh[\beta(1 - x_0)]} \tag{27}$$

and from Eq. (2), $\partial \hat{x}_i / x_e$ is given by

$$\frac{\partial \hat{x}_i}{\partial x_e} = \frac{H_{ie} v_e}{\sum_{k \in NE_i} (H_{ik} v_k)} \tag{28}$$

The derivatives of the objective and constraint functions with respect to the physical densities are presented in the following.

5.1.1 Derivative of compliance and material volume

The derivative of the objective function with respect to the physical densities becomes:

$$\frac{\partial C}{\partial \hat{x}_i} = -\mathbf{U}^T \left(\frac{\partial \mathbf{K}}{\partial \hat{x}_i} \right) \mathbf{U} = -p(E_0 - E_{min}) \left(\hat{x}_i \right)^{p-1} \mathbf{u}_i^T \mathbf{k}_{0,i} \mathbf{u}_i \tag{29}$$

The normalized volume constraint is formulated as

$$\bar{V} = \frac{V(\hat{\mathbf{x}})}{f \cdot V_0} - 1 \leq 0 \tag{30}$$

Then, the derivative of the volume constraint with respect to the physical densities reads:

$$\frac{\partial \bar{V}}{\partial \hat{x}_i} = \frac{\partial V(\hat{\mathbf{x}})}{\partial \hat{x}_i} \frac{1}{f \cdot V_0} = \frac{v_i}{f \cdot V_0} \tag{31}$$

5.1.2 Derivative of stress constraints

For stress evaluation region Ω_r , the derivative of the corrected P-norm stress constraint, Eq. (12), with respect to the physical densities is expressed as

$$\frac{\partial \sigma_r^{PN}}{\partial \hat{x}_i} = c_r^s \cdot \frac{\partial \sigma_r^{PN}}{\partial \hat{x}_i} = c_r^s \cdot \sum_{a \in \Omega_r} \frac{\partial \sigma_r^{PN}}{\partial \sigma_a^{vM}} \left(\frac{\partial \sigma_r^{vM}}{\partial \sigma_a} \right)^T \frac{\partial \sigma_a}{\partial \hat{x}_i} \tag{32}$$

where the derivative of the normalized P-norm stress constraint, Eq. (9), with respect to the von Mises equivalent stress is given by

$$\frac{\partial \sigma_r^{PN}}{\partial \sigma_a^{vM}} = \frac{1}{\bar{\sigma}} \left[\sum_{a \in \Omega_r} \left(\frac{\sigma_a^{vM}}{\bar{\sigma}} \right)^{ps} \right]^{\left(\frac{1}{ps} - 1\right)} \left(\frac{\sigma_a^{vM}}{\bar{\sigma}} \right)^{(ps-1)} \tag{33}$$

Based on Eq. (5), one can obtain the derivative of the von Mises equivalent stress as

$$\frac{\partial \sigma_a^{vM}}{\partial \sigma_a} = \frac{\mathbf{V} \sigma_a}{\sigma_a^{vM}} \tag{34}$$

From Eq. (4), the term $\partial \sigma_a / \partial \hat{x}_i$ is given by

$$\begin{aligned} \frac{\partial \sigma_a}{\partial \hat{x}_i} &= q \left(\hat{x}_a \right)^{(q-1)} \delta_{ia} \mathbf{D}_0 \mathbf{B}_a^c \mathbf{u}_a + \left(\hat{x}_a \right)^q \mathbf{D}_0 \mathbf{B}_a^c \frac{\partial \mathbf{u}_a}{\partial \hat{x}_i} \\ &= q \left(\hat{x}_a \right)^{(q-1)} \delta_{ia} \mathbf{D}_0 \mathbf{B}_a^c \mathbf{u}_a + \left(\hat{x}_a \right)^q \mathbf{D}_0 \mathbf{B}_a^c \mathbf{L}_a \frac{\partial \mathbf{U}}{\partial \hat{x}_i} \end{aligned} \tag{35}$$

where δ_{ia} is the Kronecker's delta, and \mathbf{L}_a is a matrix that gathering the nodal displacements of element a from the global displacement vector abiding $\mathbf{u}_a = \mathbf{L}_a \mathbf{U}$.

From the derivative of the equilibrium equation $\mathbf{K}\mathbf{U} = \mathbf{F}$ with respect to the physical densities, we have the derivatives

of the nodal displacements as

$$\frac{\partial \mathbf{U}}{\partial \hat{x}_i} = \mathbf{K}^{-1} \left(\frac{\partial \mathbf{F}}{\partial \hat{x}_i} - \frac{\partial \mathbf{K}}{\partial \hat{x}_i} \mathbf{U} \right) \tag{36}$$

Substituting Eqs. (35) and (36) into Eq. (32) results in

$$\begin{aligned} \frac{\partial \sigma_r^{PN}}{\partial \hat{x}_i} &= c_r^s \cdot \left\{ \sum_{a \in \Omega_r} \frac{\partial \sigma_r^{PN}}{\partial \sigma_a^{vM}} \left(\frac{\partial \sigma_a^{vM}}{\partial \sigma_a} \right)^T q \left(\hat{x}_a \right)^{(q-1)} \delta_{ia} \mathbf{D}_0 \mathbf{B}_a^c \mathbf{u}_a + \left[\sum_{a \in \Omega_r} \frac{\partial \sigma_r^{PN}}{\partial \sigma_a^{vM}} \left(\frac{\partial \sigma_a^{vM}}{\partial \sigma_a} \right)^T \left(\hat{x}_a \right)^{(q)} \mathbf{D}_0 \mathbf{B}_a^c \mathbf{L}_a \right] \frac{\partial \mathbf{u}}{\partial \hat{x}_i} \right\} \\ &= c_r^s \cdot \left[\sum_{a \in \Omega_r} \frac{\partial \sigma_r^{PN}}{\partial \sigma_a^{vM}} \left(\frac{\partial \sigma_a^{vM}}{\partial \sigma_a} \right)^T q \left(\hat{x}_a \right)^{(q-1)} \delta_{ia} \mathbf{D}_0 \mathbf{B}_a^c \mathbf{u}_a + \lambda_S^T \left(\frac{\partial \mathbf{F}}{\partial \hat{x}_i} - \frac{\partial \mathbf{K}}{\partial \hat{x}_i} \mathbf{U} \right) \right] \end{aligned} \tag{37}$$

where λ_s denote the adjoint vectors and are the solution of the following adjoint system:

$$\mathbf{K} \lambda_s = \sum_{a \in \Omega_r} \frac{\partial \sigma_r^{PN}}{\partial \sigma_a^{vM}} \left(\hat{x}_a \right)^{(q)} \left(\mathbf{D}_0 \mathbf{B}_a^c \mathbf{L}_a \right)^T \frac{\partial \sigma_a^{vM}}{\partial \sigma_a} \tag{38}$$

The derivative of the external load vector in Eq. (37) vanishes when the loads are independent of the material distribution.

5.1.3 Derivative of simply-connected constraint

For potential evaluation region Ω_t , the derivative of the corrected P-norm potential constraint, Eq. (24), with respect to the physical densities is given by

$$\frac{\partial \phi_t^{PN}}{\partial \hat{x}_i} = c_t^c \cdot \left(\frac{\partial \phi_t^{PN}}{\partial \hat{x}_i} \right) \tag{39}$$

where the term $\partial \phi_t^{PN} / \partial \hat{x}_i$ is formulated as

$$\frac{\partial \phi_t^{PN}}{\partial \hat{x}_i} = \sum_{b \in \Omega_t} \frac{\partial \phi_t^{PN}}{\partial \varphi_b} \frac{\partial \varphi_b}{\partial \hat{x}_i} = \left(\sum_{b \in \Omega_t} \mathbf{g}_b^T \right) \frac{\partial \mathbf{U}^\phi}{\partial \hat{x}_i} \tag{40}$$

in which

$$\mathbf{g}_b = \left[0 \quad \dots \quad 0 \quad \left(\frac{\partial \phi_t^{PN}}{\partial \varphi_b} \right) \quad 0 \quad \dots \quad 0 \right]^T \tag{41}$$

The sparse vector \mathbf{g}_b has the same dimensions as the potential vector \mathbf{U}^ϕ and is obtained by expanding the node vector to the global level. From Eq. (21), one can obtain

$$\frac{\partial \phi_t^{PN}}{\partial \varphi_b} = \frac{1}{\eta \cdot \phi_0} \left[\sum_{b \in \Omega_t} \left(\frac{\varphi_b}{\eta \cdot \phi_0} \right)^{pc} \right]^{\left(\frac{1}{pc} - 1 \right)} \left(\frac{\varphi_b}{\eta \cdot \phi_0} \right)^{pc-1} \tag{42}$$

From the derivative of $\mathbf{K}^\phi \mathbf{U}^\phi = \mathbf{F}^\phi$ with respect to the physical densities, we have

$$\frac{\partial \mathbf{U}^\phi}{\partial \hat{x}_i} = \left(\mathbf{K}^\phi \right)^{-1} \left(\frac{\partial \mathbf{F}^\phi}{\partial \hat{x}_i} - \frac{\partial \mathbf{K}^\phi}{\partial \hat{x}_i} \mathbf{U}^\phi \right) \tag{43}$$

Then, by the adjoint method, Eq. (40) is rewritten as

$$\begin{aligned} \frac{\partial \phi_t^{PN}}{\partial \hat{x}_i} &= \left(\sum_{b \in \Omega_t} \mathbf{g}_b^T \right) \left(\mathbf{K}^\phi \right)^{-1} \left(\frac{\partial \mathbf{F}^\phi}{\partial \hat{x}_i} - \frac{\partial \mathbf{K}^\phi}{\partial \hat{x}_i} \mathbf{U}^\phi \right) \\ &= \lambda_c^T \left(\frac{\partial \mathbf{F}^\phi}{\partial \hat{x}_i} - \frac{\partial \mathbf{K}^\phi}{\partial \hat{x}_i} \mathbf{U}^\phi \right) \end{aligned} \tag{44}$$

where λ_c denote the adjoint vectors and are the solution of the following adjoint system:

$$\mathbf{K}^\phi \lambda_c = \sum_{b \in \Omega_t} \mathbf{g}_b \tag{45}$$

From Eqs. (18) and (19), one can obtain

$$\begin{cases} \frac{\partial \mathbf{K}^\phi}{\partial \hat{x}_i} = -pe(1-\hat{x}_i)^{pe-1} (\varepsilon_v^\phi - \varepsilon_s^\phi) \mathbf{K}_{0,i}^\phi \\ \frac{\partial \mathbf{F}^\phi}{\partial \hat{x}_i} = -\rho_v^\phi \mathbf{F}_{0,i}^\phi \end{cases} \tag{46}$$

5.2 Optimization process

The optimization procedure is presented in Fig. 1. Following this idea, a simplified flow chart in pseudo-code may be described as:

Step 1: Initialize optimization parameters, including finite element mesh, material properties, termination criteria, loop parameters, and MMA optimizer setting.

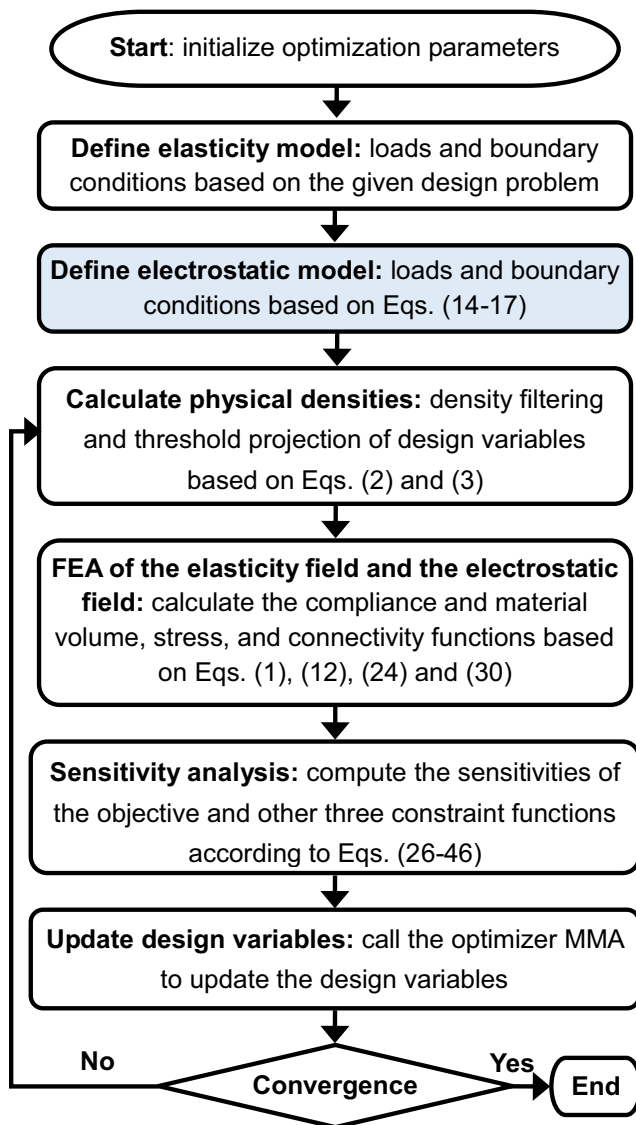


Fig. 1 Flowchart of the optimization process

- Step 2: Define optimization models, including the elasticity model for the mechanical analysis, and the corresponding electrostatic model for the simply-connected constraint according to Eqs. (14–17).
- Step 3: Calculate the physical densities by the density filtering and threshold projection of design variables according to Eqs. (2) and (3).
- Step 4: Execute the finite element analysis (FEA) of the elastic mechanics field and the electrostatic field, compute the objective and constraint functions by the physical densities according to Eqs. (1), (12), (24), and (30).
- Step 5: Sensitivity analysis of the objective and constraint functions using the chain rule and the adjoint method according to Eqs. (26–46).
- Step 6: Update the design variables by MMA.

Step 7: Repeat steps 3 ~ 6 until the result meets the convergence criterion and stop.

It can be seen from Fig. 1 that the solution of the relatively complex MCVSC problem in each iteration involves the solution of two different equilibrium problems. Firstly, the general elastic equilibrium problem is solved to obtain the nodal displacements, and then the sensitivity of compliance and volume constraint is directly calculated. Besides, the adjoint problem analysis is carried out for each region of aggregated stress constraints to get the sensitivity information of stress constraints. Next, the electrostatic model-based electrostatic equilibrium problem is solved to get the nodal potentials. Accordingly, the adjoint problem is analyzed for each region of aggregated potential constraints to produce the sensitivity information of the potential constraint.

Clearly, for such a multi-field and multi-constraint topology optimization problem (i.e., MCVSC), new and effective optimization method, such as the material-field series-expansion method (Luo and Bao 2019; Luo et al. 2020), may be very helpful to improve the computational efficiency of this problem in the future study.

6 Numerical examples

The purpose of this section is to present the numerical study on the proposed MCVSC formulation and the corresponding algorithm through a series of benchmark tests. Plane stress problems with unit thickness are assumed, and discretized by regular meshes of four-node bilinear square finite element.

In all the examples, the Young's modulus and Poisson's ratio are set to be $E_0 = 1$ and $\nu = 0.3$, respectively, for the fully solid material. The filter radius is $r_{\min} = 3.5$. The stress-related optimization parameters are listed in Tables 2 and 3 as a reference, also the EPC factor. In the EPC, the aggregation parameter is $pc = 6$ and the total number of regions is $Q = 2$. For simplicity, all domain boundaries are set to EPC boundaries unless specified otherwise, as originally suggested in (Liu et al. 2015). The MMA optimizer is carried out with default settings, except for a reduced initial move limit of 0.1. Besides, the lower limit of the design variables is set as 0.001 for avoiding numerical problems caused by zero density values. The optimization process will terminate, when the maximum change in the design variables between consecutive iterations is smaller than a predefined tolerance of $1e-3$ or the maximum number of the iteration loop reaches 200. Topologies and Von Mises stresses are illustrated in gray and color images, respectively, as shown in Fig. 2.

Table 2 Optimization parameters for numerical example 1

Fig.	C	σ_{\max}	ps	R	η	Fig.	C	σ_{\max}	ps	R	η	Fig.	C	σ_{\max}	ps	R	η
4(b)	214.28	0.60	8	14	N/A	10(c)	534.63	1.30	6	3	0.98	14(b)	558.67	1.11	6	4	0.98
4(d)	568.94	1.00	6	14	0.98	10(d)	528.17	1.40	6	2	0.98	14(c)	561.94	1.10	6	4	0.98
9(a)	308.34	1.00	6	14	0.98	13(a)	540.45	1.02	6	14	1.18	14(d)	583.69	1.08	8	5	0.98
9(b)	203.19	1.00	6	14	0.98	13(b)	519.81	1.01	6	14	1.48	14(e)	590.29	1.10	8	6	0.98
9(c)	339.29	0.75	6	14	0.98	13(c)	489.56	1.00	6	14	1.78	15(a)	459.99	1.11	6	4	1.10
9(d)	231.10	0.57	6	14	0.98	13(d)	460.22	1.01	6	14	2.08	15(b)	325.19	1.10	6	4	1.39
10(a)	554.33	1.07	6	4	0.98	13(e)	441.13	1.00	6	14	2.38	15(c)	312.48	1.10	6	4	1.58
10(b)	537.98	1.19	6	3	0.98	14(a)	559.94	1.10	6	4	0.98	15(d)	357.48	0.90	6	14	1.58

6.1 Design of an L-shape beam

In the first example, the classical design problem of an L-shape beam, Fig. 3, is considered. The top edge of the structure is clamped, and a downwards unit force is distributed over four nodes to avoid stress concentration. The design domain is discretized with 6400 elements. The material volume fraction is set to be 40% unless otherwise stated.

6.1.1 Four different results

To investigate the influences of the stress and simply-connected constraints on optimized designs, we solve the L-shape beam problem under four situations: MCV; MCVC; MCVC; and MCVSC, respectively, see Fig. 4. Among them, the minimal compliance (i.e., the maximal stiffness) is obtained when only the volume constraint is imposed, see the MCV design in Fig. 4(a). Nevertheless, this also leads to a high-stress level and poor connectivity. When the stress constraint is applied, the maximum stress of the resulting MCVC design (Fig. 4(b)) is effectively controlled with the rectangular force path in the stress concentration regions being optimized to be an obtuse-angulate one. As a side effect, however, the compliance of the MCVC design is 9.63% larger than that of the

MCV design, implying a weakened structural stiffness. The MCVC design is in line with the reports of (Holmberg et al. 2013; Suresh and Takaloozadeh 2013; Verbart et al. 2017; Xia et al. 2018) for the same benchmark problem, as shown in Fig. 5(a, b). Nonetheless, in terms of design manufacturability, neither of them can meet the connectivity requirement of the AM and TM processes due to the enclosed voids.

In the MCVC design (Fig. 4(c)), we introduce the simply-connected constraint along with the volume constraint, which implements the connectivity but fails to restrain the stress concentration in the local area. One can easily check that the MCVC design has a rectangular recess, where the maximum stress even reaches to 180.21% of the MCV design. Besides, the compliance is increased by 151.07% compared with the MCV design for this special case, which is the cost of the connectivity design.

In the last MCVSC design (Fig. 4(d)), we apply both the stress and simply-connected constraints besides the volume constraint, which results in a compromise design that satisfies the requirements for stiffness, strength, and connectivity simultaneously. For a fair comparison, the optimization parameters related to the connectivity constraint here are consistent with those in the above MCVC design. Compared with the MCVC design, the maximum stress is reduced by 42.20% at

Table 3 Optimization parameters for numerical examples 2 and 3

Ex.	Fig.	C	σ_{\max}	ps	R	η	Ex.	Fig.	C	σ_{\max}	ps	R	η
2	17(b)	299.49	0.45	8	18	N/A	3	22(a)	278.38	0.43	10	10	N/A
2	17(d)	353.39	0.60	4	22	1.00	3	22(b)	633.07	0.60	9	22	0.50
2	20(a)	348.89	0.65	4	17	1.00	3	25(a)	621.04	0.65	6	14	0.50
2	20(b)	343.97	0.70	4	14	1.00	3	25(b)	611.92	0.70	4	17	0.50
2	20(c)	337.85	0.75	4	12	1.00	3	25(c)	609.87	0.75	4	11	0.50
2	20(d)	328.89	0.80	4	11	1.00	3	25(d)	607.99	0.80	4	15	0.50

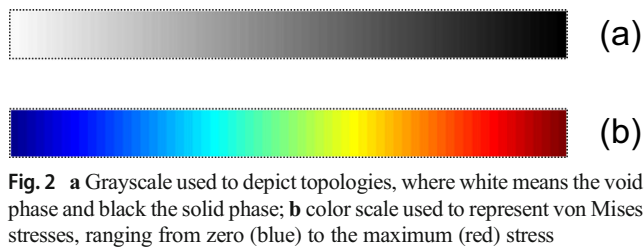


Fig. 2 **a** Grayscale used to depict topologies, where white means the void phase and black the solid phase; **b** color scale used to represent von Mises stresses, ranging from zero (blue) to the maximum (red) stress

the cost of increased compliance by only 15.94%. The MCVSC design looks like a mechanical hook, which matches the reports of (Picelli et al. 2018), as shown in Fig. 5(c, d).

Figures 6 and 7 show the detailed stress evolution of the above MCVC and MCVSC designs, respectively, which illustrate how the connectivity topology with uniform stress distribution is achieved by changing local topology distribution in the region of stress concentration. From Fig. 6, one can observe that the stress concentration runs through all the iterations in the MCVC design, except for several initial iterations such as the iteration 30. As the search range of the initial feasible region is large, several local feasible solutions could be found at the early stage. Due to the lack of necessary stress measures, however, the search for feasible regions gradually turns to the only direction of maximizing stiffness. In contrast, one can see from Fig. 7 that a uniform stress distribution is quickly achieved during the optimization process in the MCVSC design. It takes only about 60 iteration steps to get the design with the stress level close to the given stress limit.

Figure 8 plots the convergence histories of all the optimized designs in Fig. 4. Without loss of generality, only the convergence histories of the first region for the stress and simply-

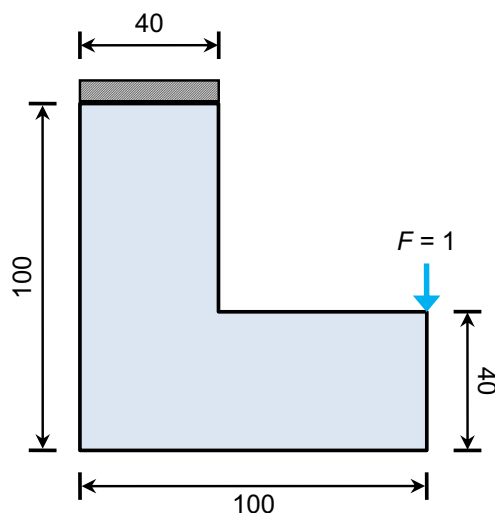


Fig. 3 Design problem of L-shape beam

connected constraints are illustrated. Except for the MCV design, some fluctuations of the objective functions can be found in the first dozens of iterations, which are mainly associated with the iterative variation of the complex stress and simply-connected constraint functions. These objective functions, however, can converge to a stable state within 50 iterations and the subsequent iterations are used to make some slight modifications of local boundary features of topologies. The validity and effectiveness of the MCVSC strategy and the corresponding solution algorithm are thus demonstrated.

Nevertheless, it should be noted that considering the aggregated stress and simply-connected constraints simultaneously will bring additional impacts to the MCVSC design. As seen in Fig. 8, the iteration oscillation of the MCVSC design is the severest, especially in the initial phase. Moreover, the convergence of the objective function for the MCVSC design is the most lagging. This is not surprising, as pointed out by (Le et al. 2010; Luo et al. 2013), one of the main disadvantages of the aggregated constraint is the high nonlinearity, which may cause unstable convergence during the optimization procedure. Clearly, compared with the design with a single aggregated constraint (i.e., the MCVC and MCVC designs), the second aggregated constraint further enhances the nonlinearity of the MCVSC design, leading to more iteration oscillations, thereby delaying the convergence.

It is shown that considering both the two aggregated constraints will have at least three impacts on the MCVSC design. Firstly, the increased computational burden from multiple constraints inevitably leads to a decrease in the computational efficiency of the design. Secondly, the convergence efficiency of the objective function slows down. Unlike the first two, however, the third may be positive. Due to the introduction of the simply-connected constraint, the initial topological configuration can be formed quickly (see Figs. 6 and 7), which may help to alleviate the severe initial oscillation of stress constraints caused by large-scale topological changes. Certainly, there may be other deeper impacts, but this would be a systematic and complex study, which is worthy of further exploration in the future.

6.1.2 Effect of different constraint limits

This section aims to illustrate the effects of the volume, stress, and simply-connected constraint limits on MCVSC designs. For a fair comparison, all the relevant researches follow the optimization condition used in the MCVSC design of Fig. 4(d).

(1) Effect of material volume limits

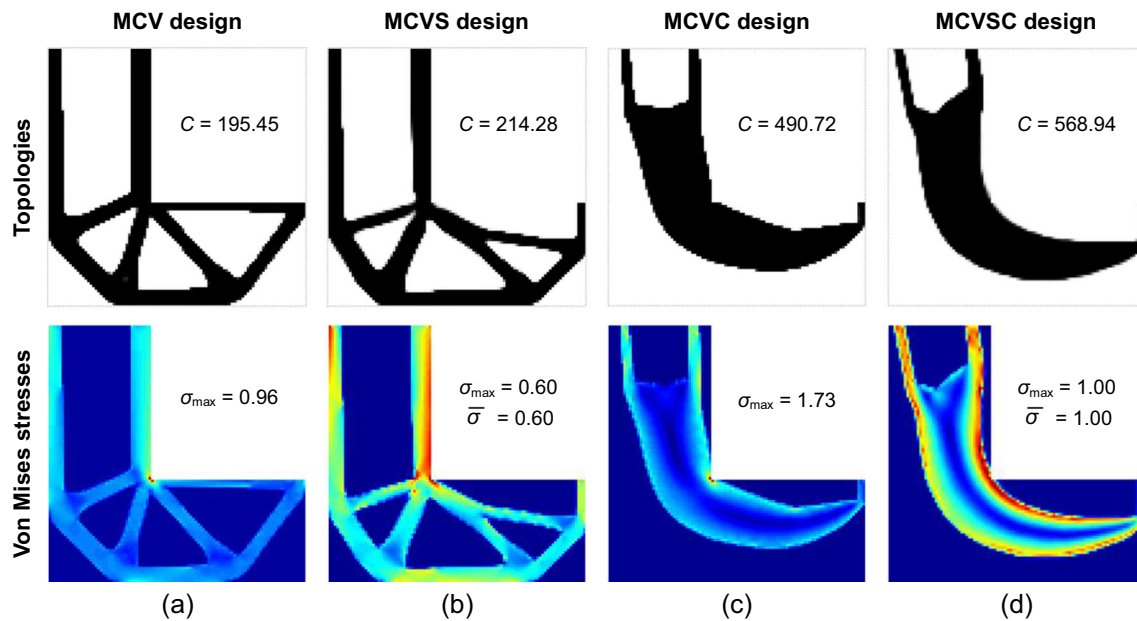


Fig. 4 Optimized designs for the four settings: MCV, MCVS, MCVC, and MCVSC

Figure 9a, b shows the MCVSC designs under different material volume fractions, which have roughly similar topologies with apparent differences in shape. Furthermore, as expected, the compliance decreases with increasing material volume fraction. However, the stress concentration is exacerbated, though the stress limit is satisfied. This is not surprising, since larger volume fractions give designs with more materials to reinforce the high-stress regions, thereby reducing their scale. It appears that larger volume fractions may help to produce MCVSC designs with higher stiffness and strength. To verify this, we tested other lower stress limits considering decremental steps of 0.01 to find the relatively high-strength designs for the two MCVSC designs. Figure 9c, d presents the rational designs finally obtained.

(2) Effect of stress limits

Figure 10 shows the MCVSC designs considering various stress limits, where all constraints are active. The optimized topologies are similar, but the geometrical shapes present slight differences, especially at the reentrant corner. One can verify that the smaller the stress limit, the more rounded becomes the reentrant corner, and the more the stresses get distributed. It also can be seen that a stricter stress limit leads to higher compliance. For illustration purposes, the compromise relation between compliance and stress limit for all MCVSC designs (Figs. 4d and 10) is depicted in Fig. 11 (red marker line), where all data are normalized with the results of the strictest stress limit.

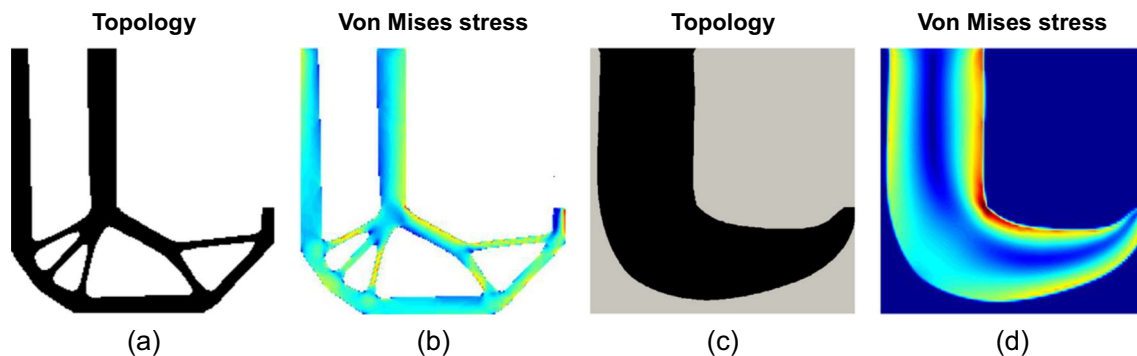


Fig. 5 Comparison of optimized designs: (a) and (b) from (Xia et al. 2018); (c) and (d) from (Picelli et al. 2018)

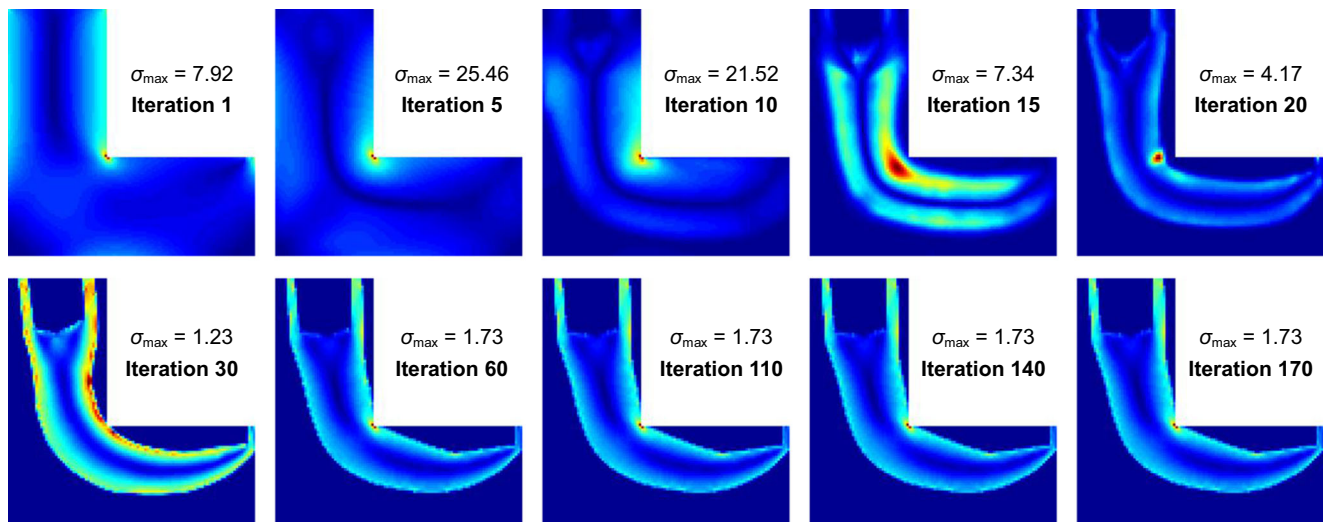


Fig. 6 Stress evolution for the MCV design of Fig. 4(c)

Next, to investigate whether the imposed stress constraint has an impact on the simply-connected constraint, we examine the change of ϕ_{\max} . Figure 12(a) depicts the variation, where the case of the MCV design and the constraint threshold (η ϕ_0) are also provided for reference. Although only a slight change in the ϕ_{\max} for this special example, it is enough to illustrate the fact that the stress constraint does have an impact on the simply-connected constraint in the MCVSC design, and this effect will vary with the constraint limits. This is reasonable because the stress constraint will exert an influence on the physical density field, thus affecting the simply-

connected constraint. It means that it is necessary to fine-tune the constraint threshold for different stress settings to achieve a high-performance MCVSC design.

(3) Effect of simply-connected constraint limits

Figure 13 shows the MCVSC designs with different potential limits. For a fixed reference threshold, varying potential limits are reflected by different values of the EPC factor η . One can verify that the connectivity effect declines with the increase of the values of η (highlighted by

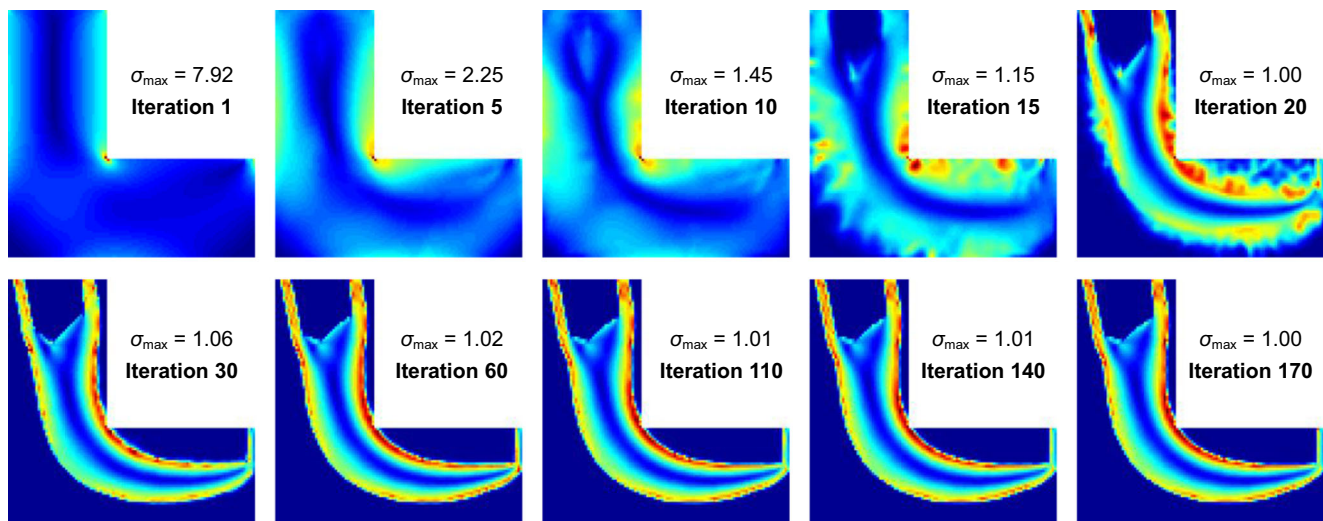
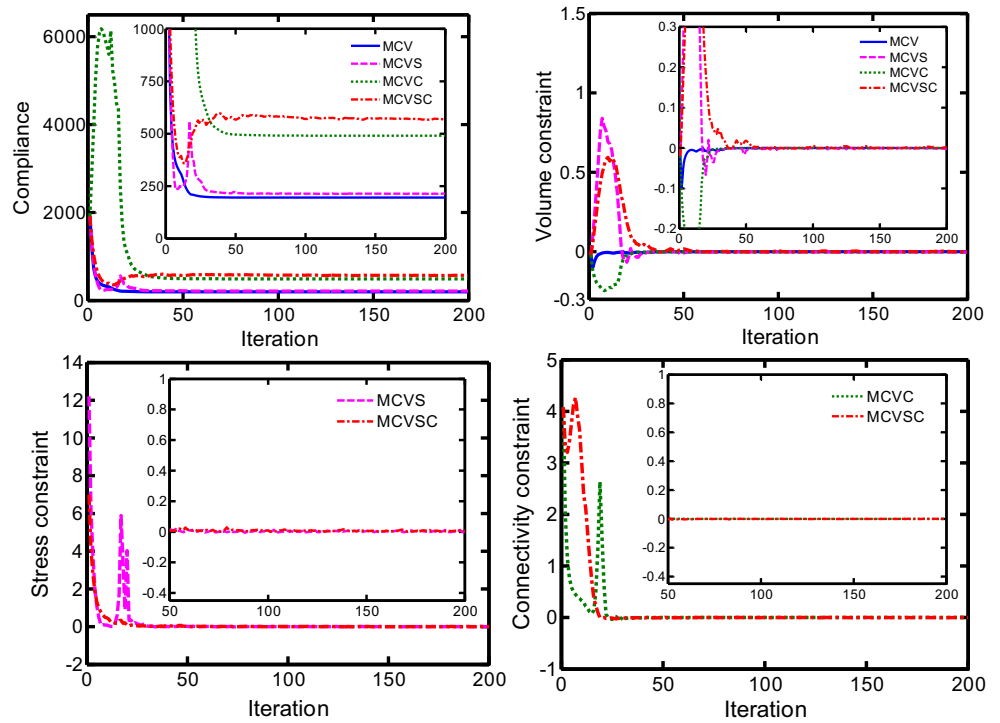


Fig. 7 Stress evolution for the MCVSC design of Fig. 4(d)

Fig. 8 Convergence histories for the MCV, MCVS, MCVC, and MCVSC designs in Fig. 4



the red dotted circles) due to the constraint threshold-dependent nature of the simply-connected constraint (Wang et al. 2020a). Nonetheless, almost all the stress constraints are satisfied, except for several slight perturbations caused by the changed connectivity designs.

6.1.3 Mesh refinement study

In this subsection, the effect of mesh refinement on MCVSC designs is discussed based on the MCVSC design case in Fig. 10(a) for comparison. The obtained results for the other three

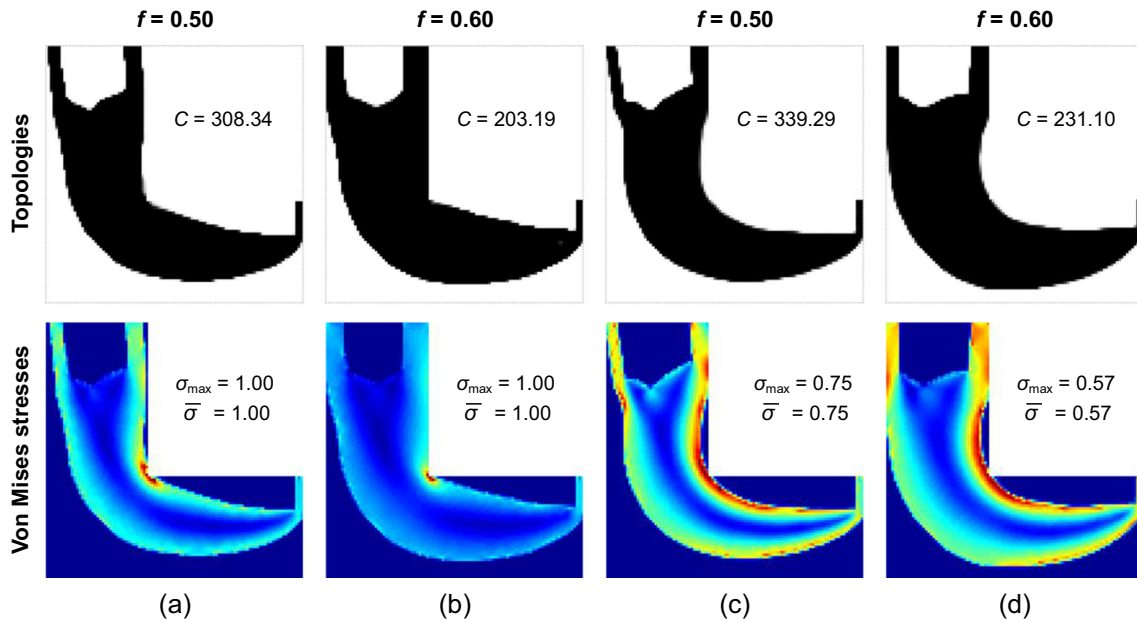


Fig. 9 MCVSC designs for volume fractions $f=0.5$ and 0.6 under different stress limits

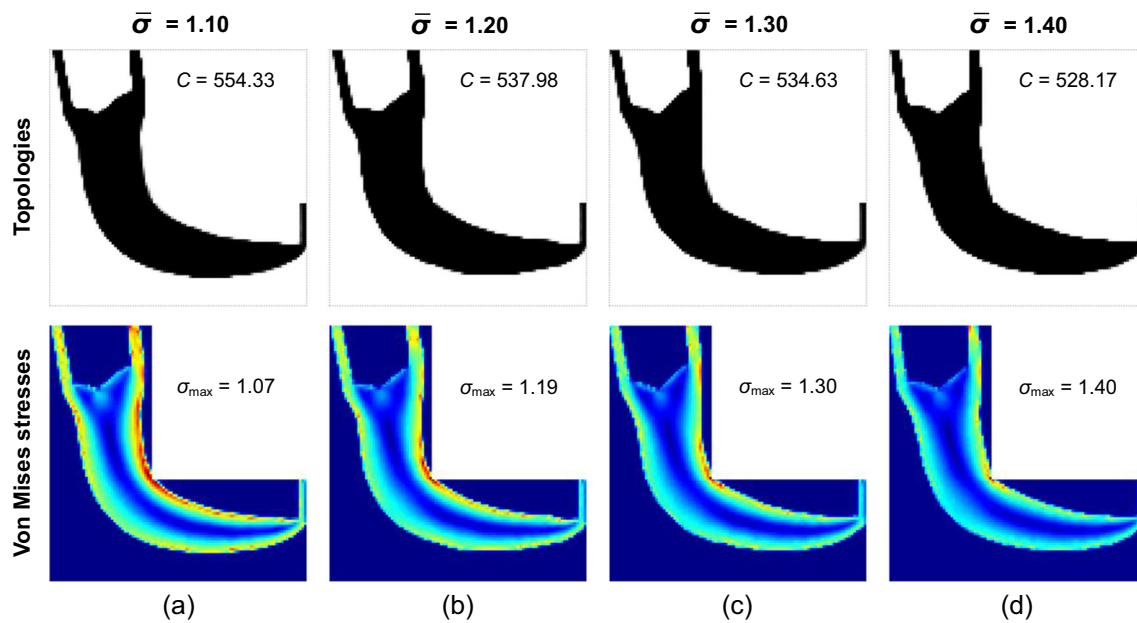


Fig. 10 MCVSC designs for stress limits $\bar{\sigma} = 1.10, 1.20, 1.30,$ and 1.40

different meshes are depicted in Fig. 14(a, b, c). It is seen that the design for the mesh with 14,400 elements has the same topology as that of Fig. 10(a). For the remaining two meshes, although similar topologies are achieved, they have failed volume constraints. This is justified since the accuracy of stress evaluation can be improved by the refined meshes. One can verify that the initial stress level σ_{\max}^1 also increases with mesh refinement. For the fixed stress limit 1.10 here, however, it means that the finer the mesh, the stricter the stress constraint. As the mesh is refined, the optimization algorithm must make

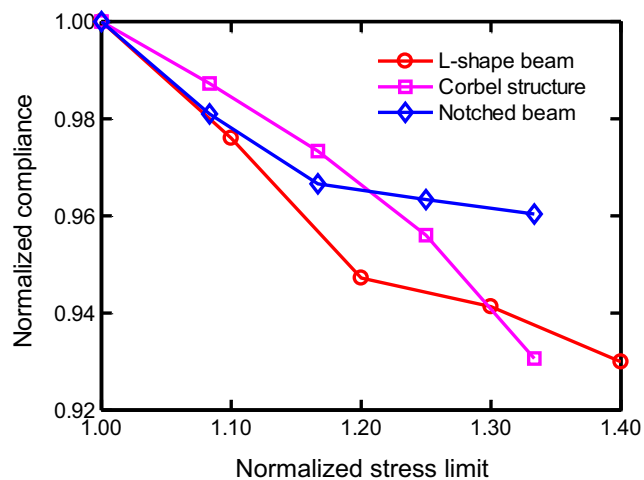


Fig. 11 Compliance changes with the stress limit for the MCVSC designs in three numerical examples

a compromise, by providing more materials to meet the increasingly strict stress constraint. Excess materials also increase the burden of the simply-connected constraint, making it ineffective (see Fig. 14(c)). On the other hand, despite the similar effect on the simply-connected constraint, the degree is quite different, or even weaker, because the constraint directly depends on simple node values. As a result, without other modifications, reasonable designs were finally achieved just by improving the stress constraint settings (increased values of ps and R can be found in Table 2), but not by modifying the simply-connected constraint, as shown in Fig. 14(d, e).

6.1.4 Influence of EPC boundary conditions

The purpose of this subsection is to illustrate the effect of EPC boundary conditions on MCVSC designs. To this end, we revisit the MCVSC optimization with different EPC boundary conditions, using the optimization parameters in Fig. 10(a). For simplicity, only three reasonable EPC boundary conditions are considered based on numerical experiments in this investigation. The values of the EPC factor η used for different boundary conditions are listed in Table 2. Figure 15(a, b, c) shows optimized results, where topologies with different shapes can be found due to the effect of boundary conditions. Among them, the smallest compliance is achieved in the case of Fig. 15(c), which is about 43.63% lower than that of Fig. 10(a). Figure 15(d) presents the result for a lower stress limit

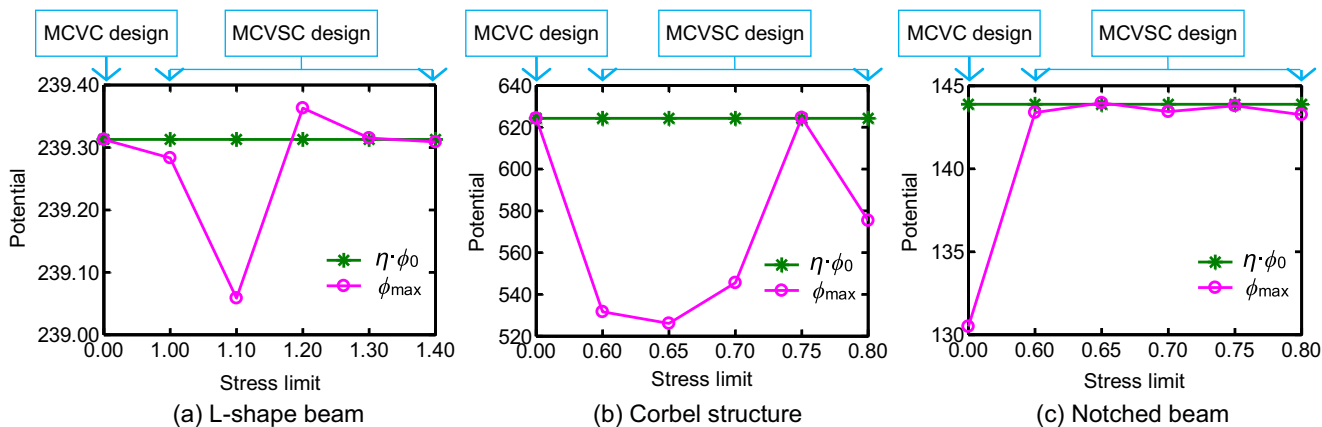


Fig. 12 Variation of the ϕ_{max} under different stress constraint conditions

corresponding to the case of Fig. 15(c), in which the stress decreased by 10% and the compliance 37.17%, compared with the case of Fig. 4(d). Unsurprisingly, the choice of EPC boundary conditions has also a significant impact on the MCVSC designs, but the essence can be attributed to the dependence of EPC-based connectivity design on EPC boundary conditions. Clearly, the self-driven method of finding the best conditions is still a valuable challenge for future work.

6.2 Design of a corbel structure

In the second example, a corbel structure (Luo et al. 2013; Yang et al. 2018) in Fig. 16 is considered. The top and bottom sides of the column are clamped and the corbel is fixed at the

middle height of the column. The concentrated load $F = 3$ is distributed equally over fifteen neighboring nodes (three layers and five nodes per layer) to avoid stress concentration. For illustration purposes, the stresses at the support regions are not considered. The design domain is discretized into 17,700 square elements. The material volume fraction is 35% unless otherwise stated.

As in the first example, the corbel problem is addressed considering four situations; see Fig. 17. Similar to the previous case, the design that only considers the volume constraint, i.e., the MCV design in Fig. 17(a), is the stiffest but has high-stress concentration and no connectivity. While the introduced stress constraint removes the two reentrant corners causing stress concentration in the MCVS design (Fig. 17(b)), the

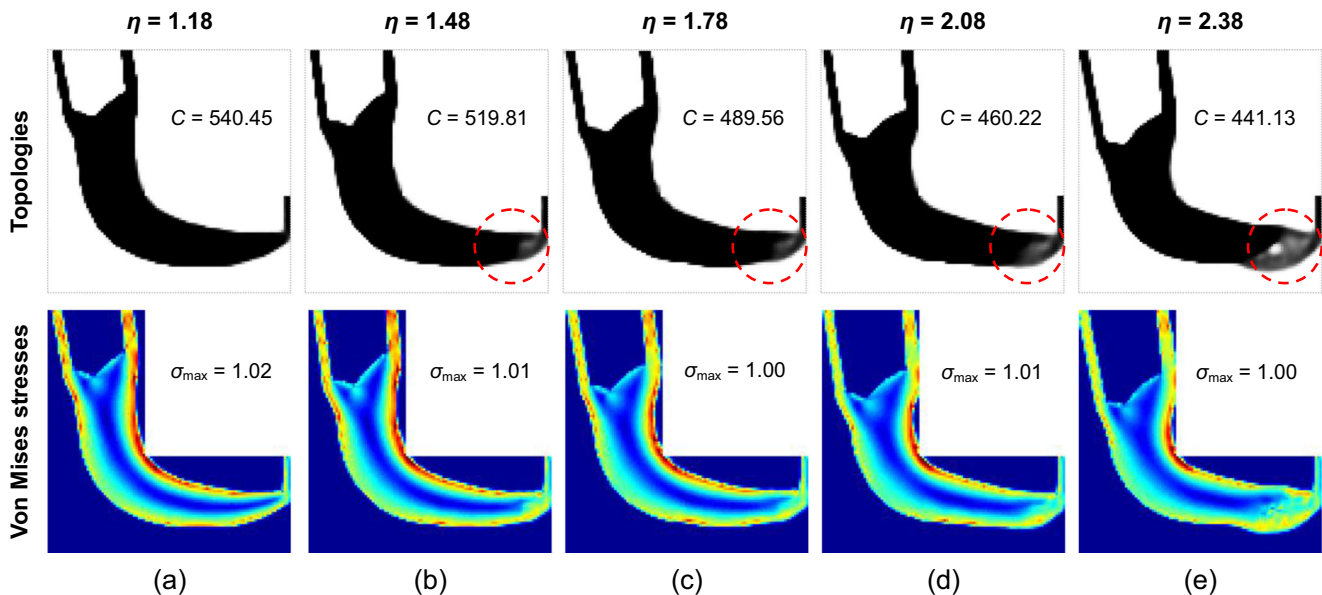


Fig. 13 MCVSC designs for $\eta = 1.18, 1.48, 1.78, 2.08,$ and 2.38 . The red dotted circles highlight the invalid areas of the connectivity constraint

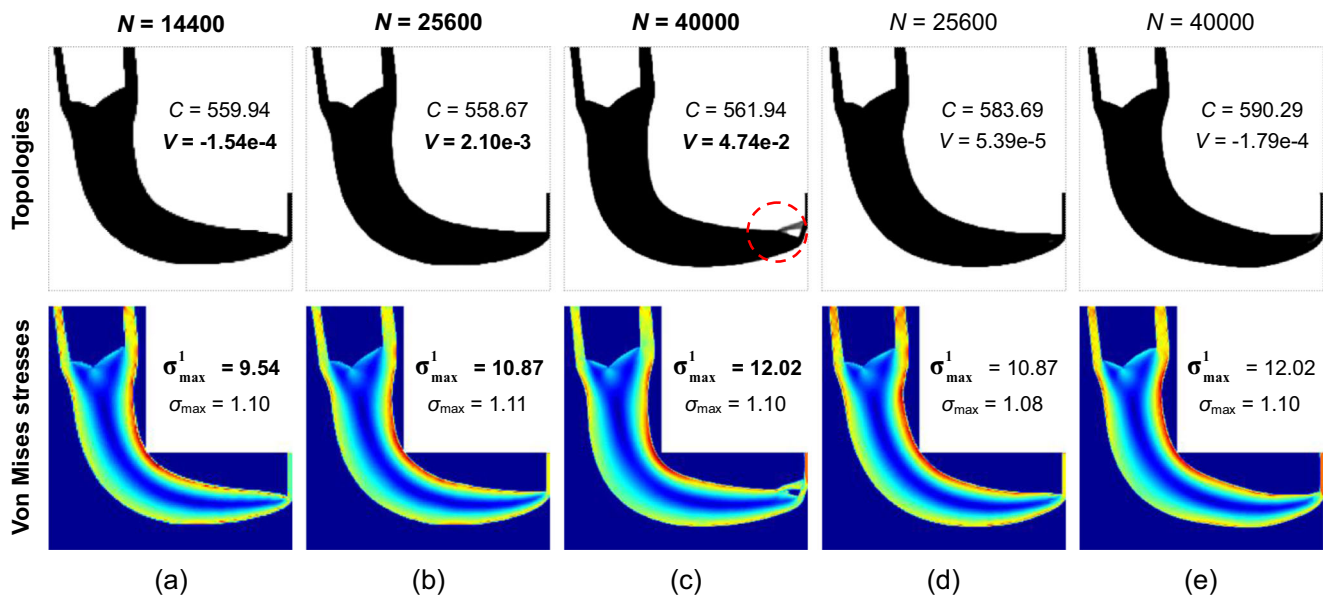


Fig. 14 MCVSC designs for different meshes, where (d, e) obtained by using the enhanced stress constraint settings as listed in Table 2. σ_{max}^1 represents the initial stress level. The red dotted circle highlights the invalid area of the connectivity constraint

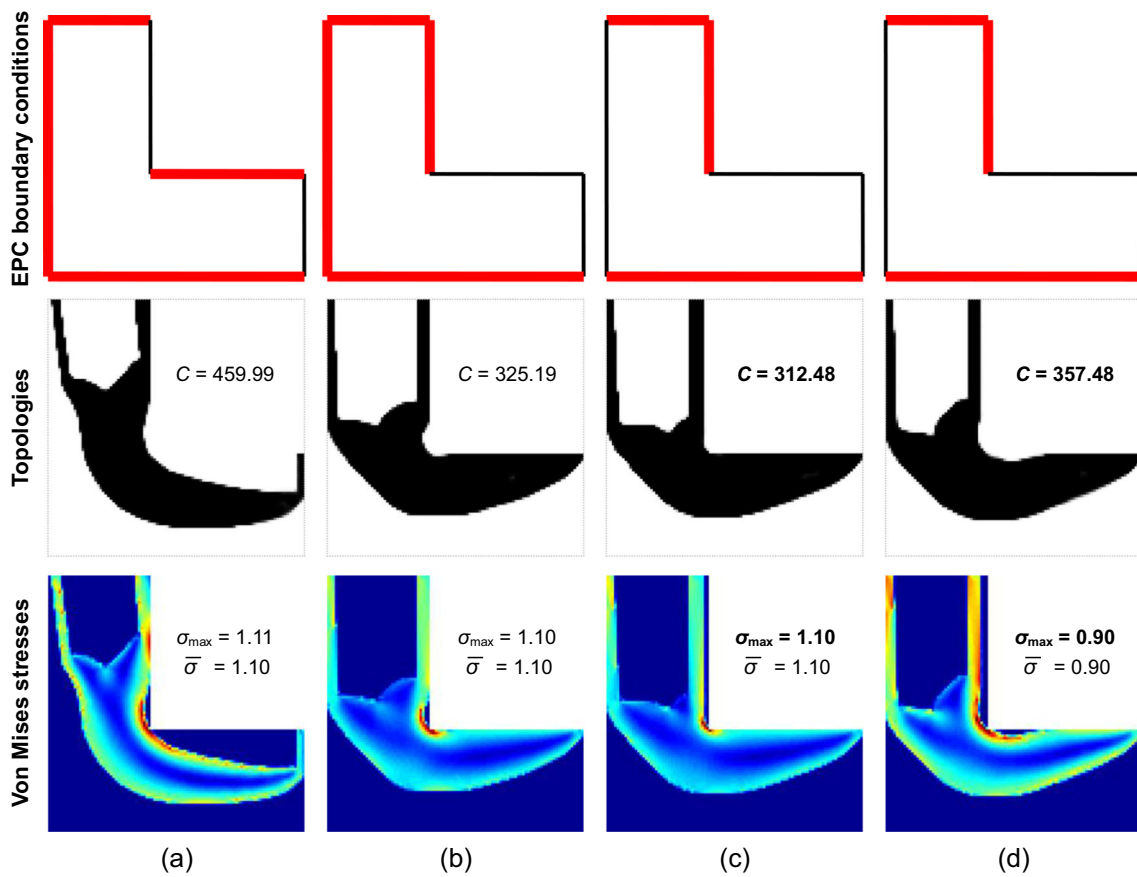


Fig. 15 MCVSC designs for different EPC boundary conditions. The EPC boundaries are highlighted by red thick lines

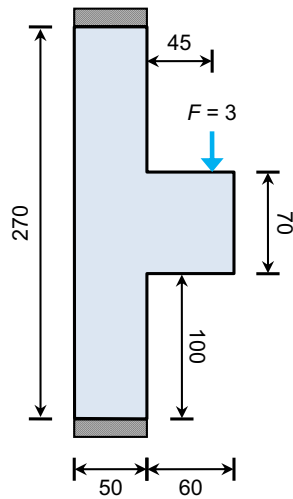


Fig. 16 Design problem of corbel structure

complex enclosed void configuration obtained makes the design difficult to fabricate when the fabricating orientations are limited in the x, y -plane. When only the volume and simply-connected constraints are applied, the resulting MCV design (Fig. 17(c)) overcomes the connectivity problem but presents weak strength. Figure 17(d) illustrates the ability of the MCVSC formulation to improve the structural performance and manufacturability by integrating all three constraints, the potential failures aroused by high-stress levels and/or manufacturing difficulties caused by enclosed voids in the other three cases are avoided. Using the proposed MCVSC setting, high requirements on strength and connectivity are satisfied at the cost of a reasonable reduction in stiffness under a given usable material volume. The MCVSC design is in line with the reports of (Luo et al. 2013; Yang et al. 2018).

Figure 18 depicts the highly efficient stress distribution of the MCVSC design, where only about 30 iterations are

Fig. 17 Optimized designs for the four settings: MCV, MCVS, MCV, and MCVSC. The red dotted circles and arrows highlight the design differences

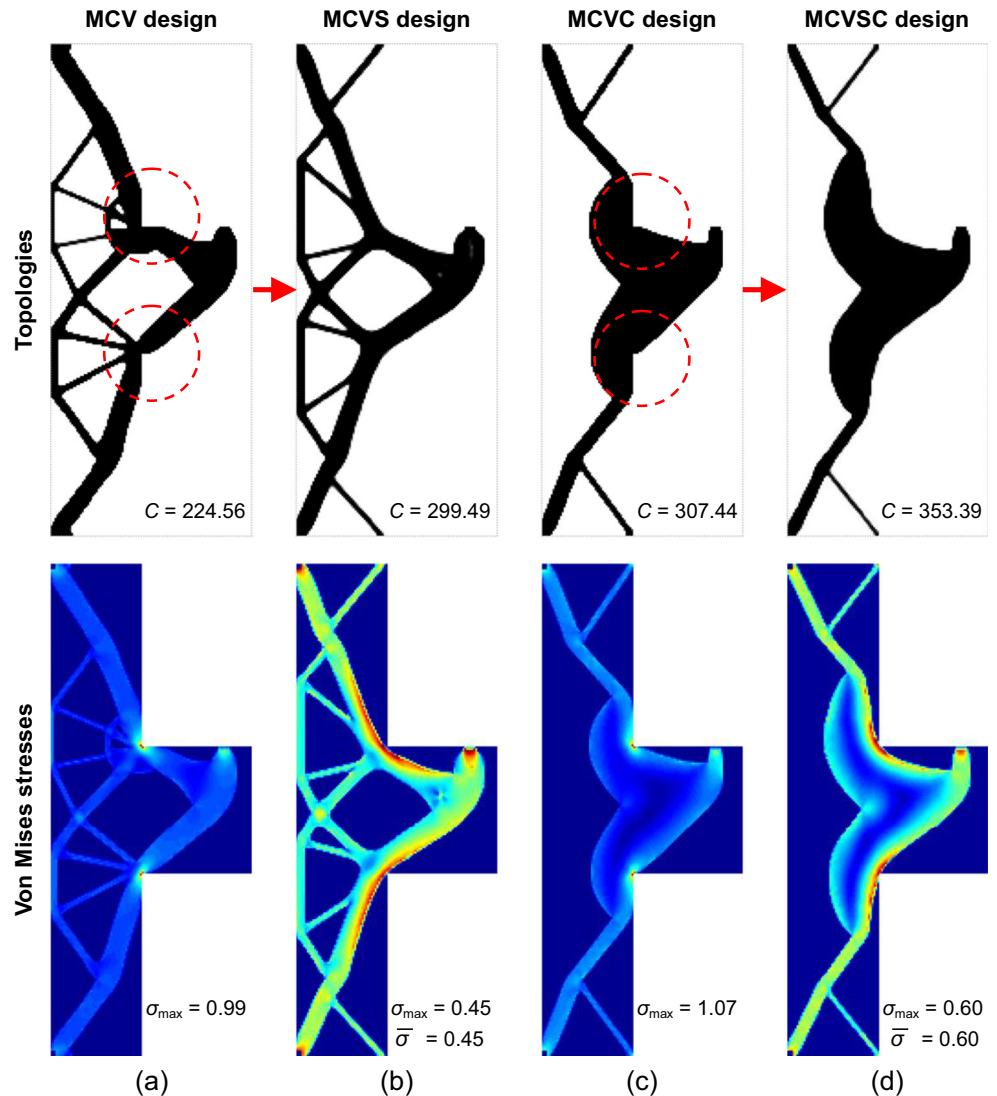
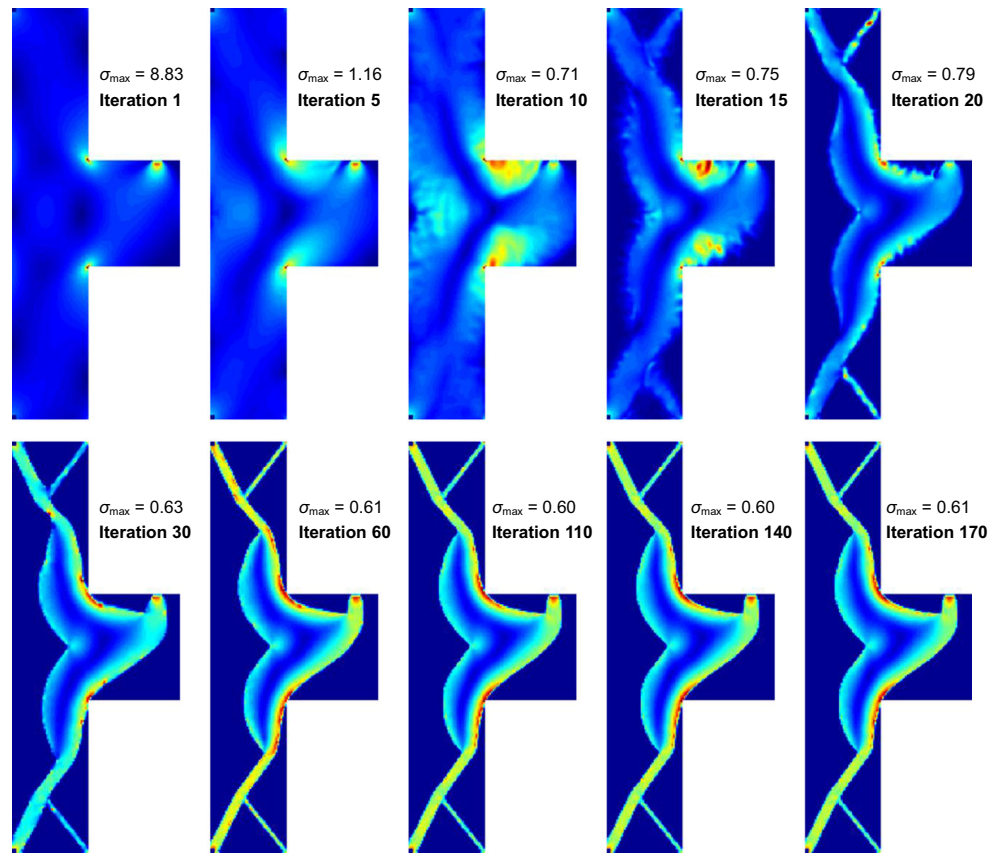


Fig. 18 Stress evolution for the MCVSC design of Fig. 17(d)



dominant in achieving the design with the stress level closes to the prescribed stress limit.

Figure 19 presents the relatively stable convergence histories for the above MCVSC design. A stricter constraint behavior can be observed for the simply-connected constraint due to the effect of the introduced stress constraint, as discussed in Section 6.1.2(2). The simply-connected constraint settings in the MCVSC design (Fig. 17(d)) are inherited from the MCVC design (Fig. 17(c)) for a fair comparison. Therefore, a fine-tune for the simply-connected constraint settings for the MCVSC design would help to obtain a more moderate constraint behavior.

Figure 20 shows the MCVSC designs with different stress limits, where all constraints are active. These designs exhibit the same behavior as observed in the L-shape beam problem: the smaller the stress limit, the more the stresses get distributed, and the higher the compliance. Figure 11 (pink marker line) illustrates the compromise relation between compliance and stress limit for all MCVSC designs (Figs. 17(d) and 20), where all data are normalized with the results of the strictest stress limit. For this special example, the obvious disturbances of the stress constraint on the simply-connected constraint can be verified in Fig. 12(b).

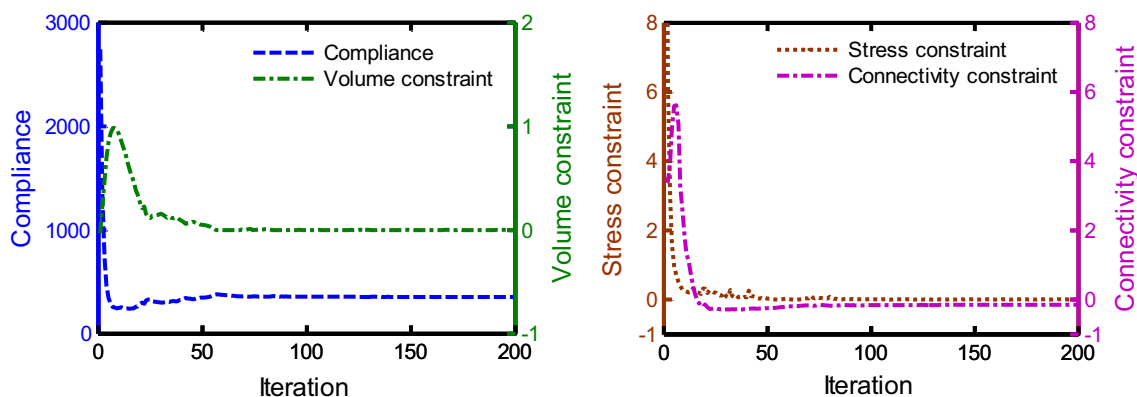
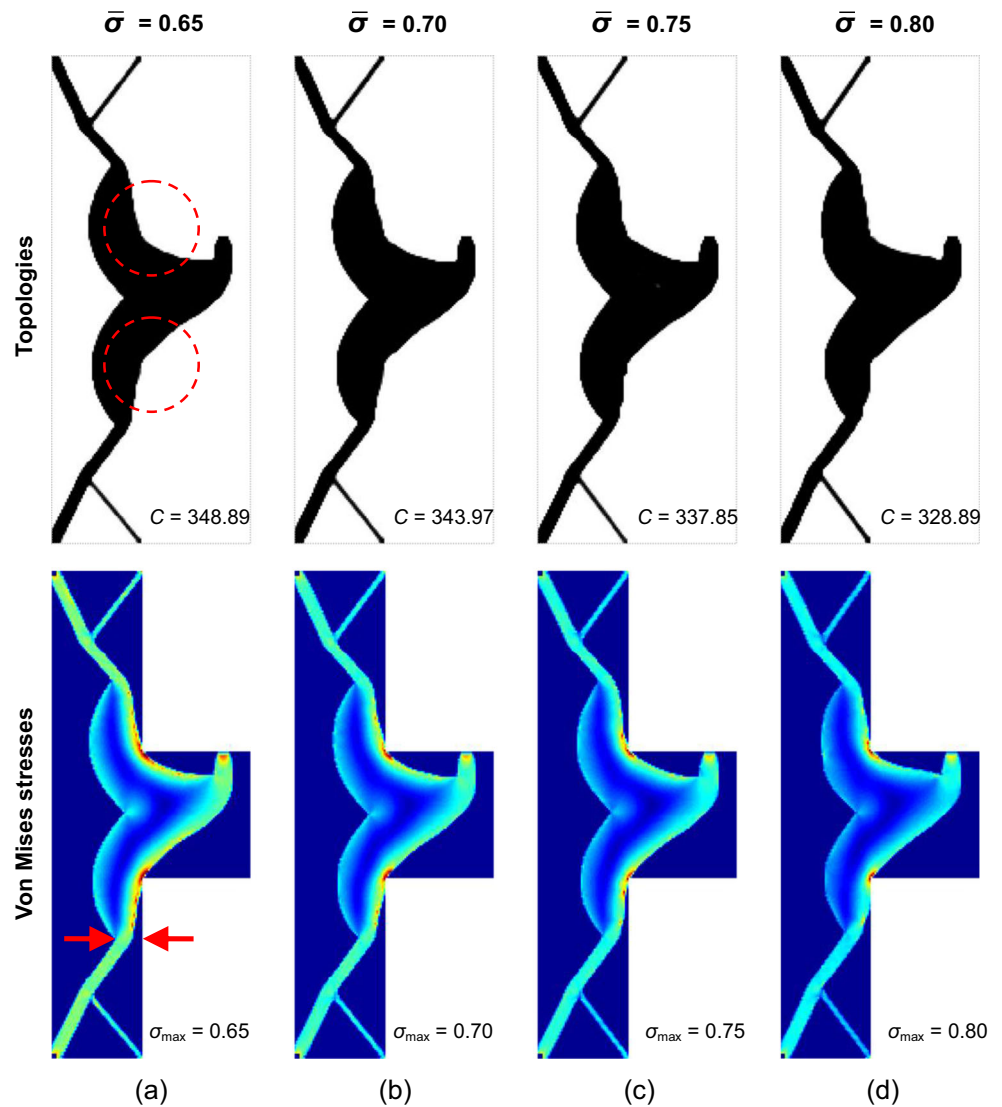


Fig. 19 Convergence histories for the MCVSC design in Fig. 17(d)

Fig. 20 MCVSC designs for stress limits $\bar{\sigma} = 0.65, 0.70, 0.75,$ and 0.80 . The red dotted circles and arrows highlight the design differences



6.3 Design of a notched beam

In the last example, a notched beam (Polajnar et al. 2017; Picelli et al. 2018) in Fig. 21 is tested, where a pre-existing vertical crack notch of height 12 located in the middle of the bottom edge. Following (Picelli et al. 2018), the stress at the loading and support regions are not considered for illustration purposes. The design domain is discretized with 11,520

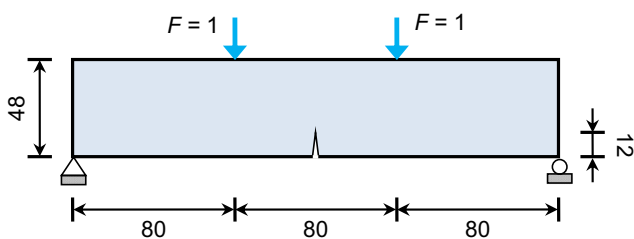


Fig. 21 Design problem of the notched beam

elements. The material volume fraction is 50% unless otherwise stated.

In the last example, as in the first two, the notched beam is solved considering four situations; see Fig. 22. Similar to the previous cases, the MCV design (Fig. 22(a)) considering the volume constraint only is the stiffest but highly stressed due to the crack notch, also no connectivity. While the MCVS design (Fig. 22(b)) greatly enlarges the reentrant corner of the crack notch region by employing the additional stress constraint, thereby alleviating the stress concentration. As for the MCVSC design (Fig. 22(c)), an apparent stress concentration can be found in the connectivity structure. Finally, a manufacturing-oriented connectivity design with uniform stresses is achieved by using the MCVSC formulation, see Fig. 22(d). This special case also illustrates the fact that higher requirements take higher costs. Figure 23 gives the detailed stress evolution of the MCVSC design, where an efficient stress distribution

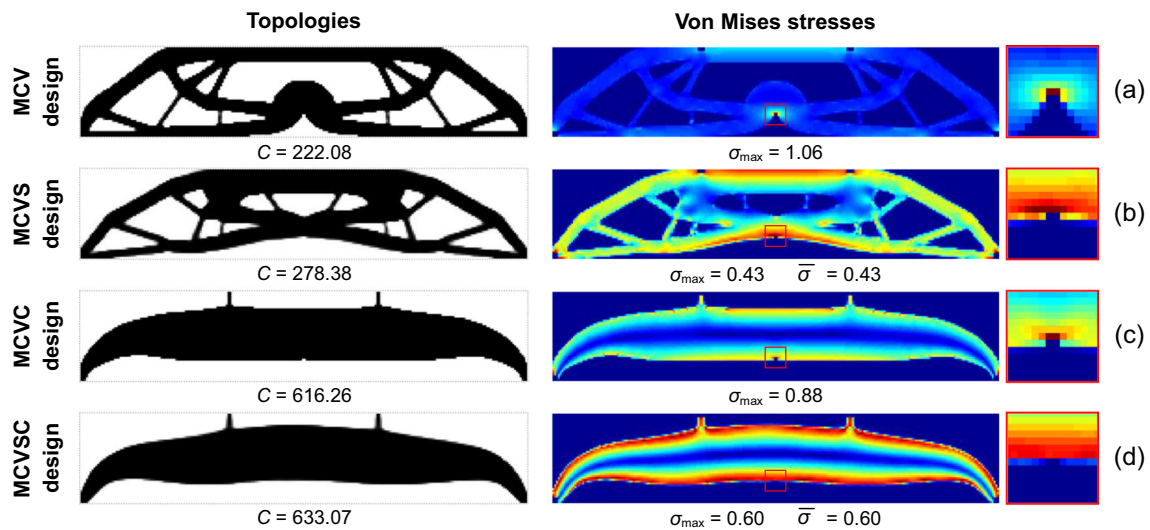


Fig. 22 Optimized designs for the four settings: MCV, MCVS, MCVC, and MCVSC

process can be checked. Figure 24 plots the stable convergence histories for the MCVSC design.

Figure 25 shows the MCVSC designs under different stress limits, where all constraints are active. The relation between compliance and stress limit for all MCVSC designs (Figs. 22(d) and 25) is in line with the previous cases, as illustrated in Fig. 11 (blue marker line), where all data are normalized with the results of the strictest stress limit. Figure 12(c) depicts the disturbances of the stress constraint on the simply-connected constraint, which make the tight constraint limit of the MCVC design is moderate for the MCVSC designs. That is why the compliance of the MCVSC design

even outperforms that of the MCVC design when the stress limit is above 0.70.

7 Concluding remarks

From a design for manufacturing point of view, not only high-performance requirements but also manufacturability should be considered in structural topology optimization for practical engineering applications. To this end, this work proposes and investigates a formulation for structural topology optimization considering practical properties of material strength, structural

Fig. 23 Stress evolution for the MCVSC design of Fig. 22(d)

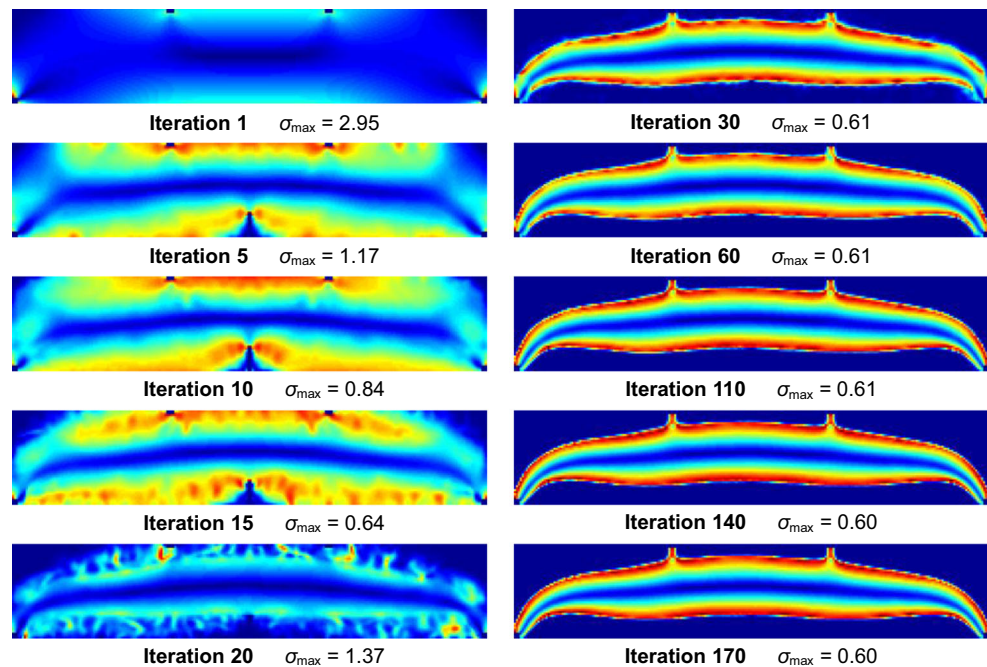
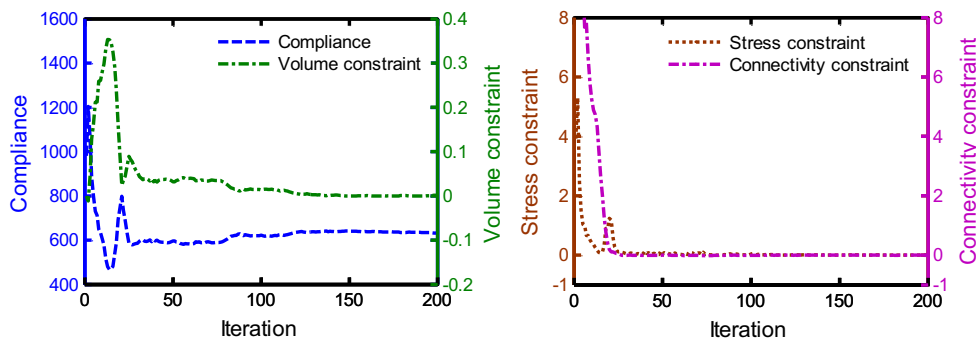


Fig. 24 Convergence histories of the MCVSC design in Fig. 22(d)



stiffness, and connectivity; viz., minimizing the compliance under the volume, stress, and simply-connected constraints. Moreover, an effective solution algorithm is developed for this relatively complex multi-constraint and multi-field problem. Benchmark examples illustrate the features of the formulation and the effectiveness of the algorithm. Some concluding remarks are drawn:

- (1) As expected, the optimized designs considering no stress and/or connectivity measures present high-stress levels and/or poor connectivity. More seriously, some pure connectivity designs even exhibit severely deteriorated stress levels. The proposed formulation is capable of providing manufacturing-friendly connectivity designs satisfying different yield stress levels with a fixed usable material volume but at the cost of compromised compliance.
- (2) The effect of the three types of constraint limits is discussed. The general fact that more material volume

is preferable for stricter design requirements is verified. Besides, the common behavior that the compliance increases with declining the stress limit is also observed. Meanwhile, the subtle influence of the stress constraint on the simply-connected constraint is demonstrated. Different from the above cases, however, the simply-connected constraint limit has a decisive impact on the resulting design, not just performance.

- (3) The study of mesh refinement confirms the influence of mesh on the obtained design. Nonetheless, improved solutions can still be achieved by fine-tuning the constraint settings for different meshes. While the research on connectivity boundary conditions illustrates the possibility for generating high-performance designs by imposing proper boundary conditions.
- (4) Various techniques are combined to overcome the numerical challenges caused by the integration of stress and simply-connected constraints. It is shown that the combination of the STM-based correction scheme and

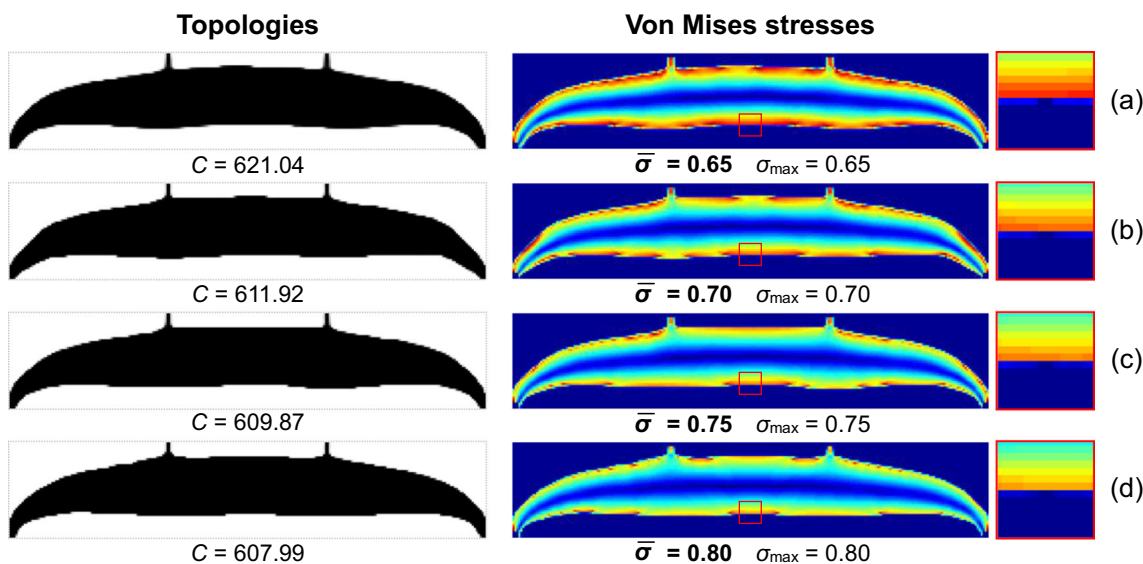


Fig. 25 MCVSC designs for stress limits $\bar{\sigma} = 0.65, 0.70, 0.75,$ and 0.80

regional measure strategy effectively handles the stress constraint and/or the simply-connected constraint.

An implementation of the formulation in three-dimensional problems would be especially valuable, which will be reported elsewhere.

Funding This work is sponsored by the National Natural Science Foundation of China (11872311, 11772070), and the Natural Science Basic Research Plan in Shaanxi Province of China (2020JM085).

Compliance with ethical standards

Conflict of interest The authors declare that they have no conflict of interest.

Replication of results Since comprehensive implementation details are provided, and the computer code belongs to a project, this code is not available here. Scientists or interested parties are welcome to contact the authors for further explanations.

References

- Bathe K-J (1996) Finite element procedures. Prentice Hall, New Jersey
- Bendsøe MP, Sigmund O (2003) Topology optimization: theory, methods and applications. Springer, Berlin Heidelberg
- Bourdin B (2001) Filters in topology optimization. *Int J Numer Methods Eng* 50:2143–2158. <https://doi.org/10.1002/nme.116>
- Bruggi M (2008) On an alternative approach to stress constraints relaxation in topology optimization. *Struct Multidiscip Optim* 36:125–141. <https://doi.org/10.1007/s00158-007-0203-6>
- Bruggi M, Duysinx P (2012) Topology optimization for minimum weight with compliance and stress constraints. *Struct Multidiscip Optim* 46:369–384. <https://doi.org/10.1007/s00158-012-0759-7>
- Bruggi M, Venini P (2008) A mixed FEM approach to stress-constrained topology optimization. *Int J Numer Methods Eng* 73:1693–1714. <https://doi.org/10.1002/nme.2138>
- Bruns TE, Tortorelli DA (2001) Topology optimization of non-linear elastic structures and compliant mechanisms. *Comput Methods Appl Mech Eng* 190:3443–3459. [https://doi.org/10.1016/S0045-7825\(00\)00278-4](https://doi.org/10.1016/S0045-7825(00)00278-4)
- Cheng GD, Guo X (1997) Epsilon-relaxed approach in structural topology optimization. *Struct Optim* 13:258–266. <https://doi.org/10.1007/BF01197454>
- CHENG G, JIANG Z (1992) Study on topology optimization with stress constraints. *Eng Optim* 20:129–148. <https://doi.org/10.1080/03052159208941276>
- da Silva GA, Beck AT, Sigmund O (2019a) Stress-constrained topology optimization considering uniform manufacturing uncertainties. *Comput Methods Appl Mech Eng* 344:512–537. <https://doi.org/10.1016/j.cma.2018.10.020>
- da Silva GA, Beck AT, Sigmund O (2019b) Topology optimization of compliant mechanisms with stress constraints and manufacturing error robustness. *Comput Methods Appl Mech Eng* 354:397–421. <https://doi.org/10.1016/j.cma.2019.05.046>
- De Leon DM, Alexandersen JO, Fonseca JS, Sigmund O (2015) Stress-constrained topology optimization for compliant mechanism design. *Struct Multidiscip Optim* 52:929–943. <https://doi.org/10.1007/s00158-015-1279-z>
- Diegel O, Singamneni S, Reay S, Withell A (2010) Tools for sustainable product design: additive manufacturing. *J Sustain Dev* 3. <https://doi.org/10.5539/jsd.v3n3p68>
- Duysinx P, Bendsøe MP (1998) Topology optimization of continuum structures with local stress constraints. *Int J Numer Methods Eng* 43:1453–1478. [https://doi.org/10.1002/\(SICI\)1097-0207\(19981230\)43:8<1453::AID-NME480>3.0.CO;2-2](https://doi.org/10.1002/(SICI)1097-0207(19981230)43:8<1453::AID-NME480>3.0.CO;2-2)
- Duysinx P, Sigmund O (1998) New developments in handling stress constraints in optimal material distribution. In: 7th AIAA/USAF/NASA/ISSMO Symposium on Multidisciplinary Analysis and Optimization. American Institute of Aeronautics and Astronautics, Reston, Virginia, pp 1501–1509
- Duysinx P, Van Miegroet L, Lemaire E et al (2008) Topology and generalized shape optimization: why stress constraints are so important? *Int J Simul Multidiscip Des Optim* 2:253–258. <https://doi.org/10.1051/ijsmdo/2008034>
- Eschenauer HA, Olhoff N (2001) Topology optimization of continuum structures: a review*. *Appl Mech Rev* 54:331–390. <https://doi.org/10.1115/1.1388075>
- Fancello EA (2006) Topology optimization for minimum mass design considering local failure constraints and contact boundary conditions. *Struct Multidiscip Optim* 32:229–240. <https://doi.org/10.1007/s00158-006-0019-9>
- Gao W, Zhang Y, Ramanujan D et al (2015) The status, challenges, and future of additive manufacturing in engineering. *Comput Des* 69:65–89. <https://doi.org/10.1016/j.cad.2015.04.001>
- Gao X, Li Y, Ma H, Chen G (2020) Improving the overall performance of continuum structures: a topology optimization model considering stiffness, strength and stability. *Comput Methods Appl Mech Eng* 359:112660. <https://doi.org/10.1016/j.cma.2019.112660>
- Gersborg AR, Andreasen CS (2011) An explicit parameterization for casting constraints in gradient driven topology optimization. *Struct Multidiscip Optim* 44:875–881. <https://doi.org/10.1007/s00158-011-0632-0>
- Guest JK, Prévost JH, Belytschko T (2004) Achieving minimum length scale in topology optimization using nodal design variables and projection functions. *Int J Numer Methods Eng* 61:238–254. <https://doi.org/10.1002/nme.1064>
- Guest JK, Asadpoure A, Ha S-H (2011) Eliminating beta-continuation from Heaviside projection and density filter algorithms. *Struct Multidiscip Optim* 44:443–453. <https://doi.org/10.1007/s00158-011-0676-1>
- Guo X, Zhang WS, Wang MY, Wei P (2011) Stress-related topology optimization via level set approach. *Comput Methods Appl Mech Eng* 200:3439–3452. <https://doi.org/10.1016/j.cma.2011.08.016>
- Holmberg E, Torstenfelt B, Klarbring A (2013) Stress constrained topology optimization. *Struct Multidiscip Optim* 48:33–47. <https://doi.org/10.1007/s00158-012-0880-7>
- Hutmacher DW, Schantz T, Zein I et al (2001) Mechanical properties and cell cultural response of polycaprolactone scaffolds designed and fabricated via fused deposition modeling. *J Biomed Mater Res* 55:203–216. [https://doi.org/10.1002/1097-4636\(200105\)55:2<203::AID-JBM1007>3.0.CO;2-7](https://doi.org/10.1002/1097-4636(200105)55:2<203::AID-JBM1007>3.0.CO;2-7)
- Jin J (2014) The finite element method in electromagnetics, 3rd edn. Wiley-IEEE Press, New Jersey
- Kruth J, Mercelis P, Van Vaerenbergh J et al (2005) Binding mechanisms in selective laser sintering and selective laser melting. *Rapid Prototyp J* 11:26–36. <https://doi.org/10.1108/13552540510573365>
- Langelær M (2019) Topology optimization for multi-axis machining. *Comput Methods Appl Mech Eng* 351:226–252. <https://doi.org/10.1016/j.cma.2019.03.037>
- Le C, Norato J, Bruns T et al (2010) Stress-based topology optimization for continua. *Struct Multidiscip Optim* 41:605–620. <https://doi.org/10.1007/s00158-009-0440-y>

- Li Q, Chen W, Liu S, Tong L (2016) Structural topology optimization considering connectivity constraint. *Struct Multidiscip Optim* 54: 971–984. <https://doi.org/10.1007/s00158-016-1459-5>
- Li Q, Chen W, Liu S, Fan H (2018) Topology optimization design of cast parts based on virtual temperature method. *Comput Des* 94:28–40. <https://doi.org/10.1016/j.cad.2017.08.002>
- Liang QQ, Xie YM, Steven GP (1999) Optimal selection of topologies for the minimum-weight design of continuum structures with stress constraints. *Proc Inst Mech Eng Part C J Mech Eng Sci* 213:755–762. <https://doi.org/10.1243/0954406991522374>
- Liu J, Ma Y (2016) A survey of manufacturing oriented topology optimization methods. *Adv Eng Softw* 100:161–175. <https://doi.org/10.1016/j.advengsoft.2016.07.017>
- Liu S, Li Q, Chen W et al (2015) An identification method for enclosed voids restriction in manufacturability design for additive manufacturing structures. *Front Mech Eng* 10:126–137. <https://doi.org/10.1007/s11465-015-0340-3>
- Liu J, Gaynor AT, Chen S et al (2018) Current and future trends in topology optimization for additive manufacturing. *Struct Multidiscip Optim* 57:2457–2483. <https://doi.org/10.1007/s00158-018-1994-3>
- Luo Y, Bao J (2019) A material-field series-expansion method for topology optimization of continuum structures. *Comput Struct* 225: 106122. <https://doi.org/10.1016/j.compstruc.2019.106122>
- Luo Y, Kang Z (2012) Topology optimization of continuum structures with Drucker–Prager yield stress constraints. *Comput Struct* 90–91: 65–75. <https://doi.org/10.1016/j.compstruc.2011.10.008>
- Luo Y, Wang MY, Kang Z (2013) An enhanced aggregation method for topology optimization with local stress constraints. *Comput Methods Appl Mech Eng* 254:31–41. <https://doi.org/10.1016/j.cma.2012.10.019>
- Luo Y, Xing J, Niu Y et al (2017) Wrinkle-free design of thin membrane structures using stress-based topology optimization. *J Mech Phys Solids* 102:277–293. <https://doi.org/10.1016/j.jmps.2017.02.003>
- Luo Y, Xing J, Kang Z (2020) Topology optimization using material-field series expansion and Kriging-based algorithm: an effective non-gradient method. *Comput Methods Appl Mech Eng* 364: 112966. <https://doi.org/10.1016/j.cma.2020.112966>
- París J, Navarrina F, Colominas I, Casteleiro M (2009) Topology optimization of continuum structures with local and global stress constraints. *Struct Multidiscip Optim* 39:419–437. <https://doi.org/10.1007/s00158-008-0336-2>
- París J, Navarrina F, Colominas I, Casteleiro M (2010) Block aggregation of stress constraints in topology optimization of structures. *Adv Eng Softw* 41:433–441. <https://doi.org/10.1016/j.advengsoft.2009.03.006>
- Pereira JT, Fancello EA, Barcellos CS (2004) Topology optimization of continuum structures with material failure constraints. *Struct Multidiscip Optim* 26:50–66. <https://doi.org/10.1007/s00158-003-0301-z>
- Picelli R, Townsend S, Brampton C et al (2018) Stress-based shape and topology optimization with the level set method. *Comput Methods Appl Mech Eng* 329:1–23. <https://doi.org/10.1016/j.cma.2017.09.001>
- Polajnar M, Kosel F, Drazumeric R (2017) Structural optimization using global stress-deviation objective function via the level-set method. *Struct Multidiscip Optim* 55:91–104. <https://doi.org/10.1007/s00158-016-1475-5>
- Qian X (2017) Undercut and overhang angle control in topology optimization: a density gradient based integral approach. *Int J Numer Methods Eng* 111:247–272. <https://doi.org/10.1002/nme.5461>
- Rozvany GIN (2009) A critical review of established methods of structural topology optimization. *Struct Multidiscip Optim* 37:217–237. <https://doi.org/10.1007/s00158-007-0217-0>
- Sigmund O (1997) On the design of compliant mechanisms using topology optimization*. *Mech Struct Mach* 25:493–524. <https://doi.org/10.1080/08905459708945415>
- Sigmund O (2007) Morphology-based black and white filters for topology optimization. *Struct Multidiscip Optim* 33:401–424. <https://doi.org/10.1007/s00158-006-0087-x>
- Sigmund O, Maute K (2013) Topology optimization approaches. *Struct Multidiscip Optim* 48:1031–1055. <https://doi.org/10.1007/s00158-013-0978-6>
- Sigmund O, Petersson J (1998) Numerical instabilities in topology optimization: a survey on procedures dealing with checkerboards, mesh-dependencies and local minima. *Struct Optim* 16:68–75. <https://doi.org/10.1007/BF01214002>
- Suresh K, Takaloozadeh M (2013) Stress-constrained topology optimization: a topological level-set approach. *Struct Multidiscip Optim* 48:295–309. <https://doi.org/10.1007/s00158-013-0899-4>
- Svanberg K (1987) The method of moving asymptotes—a new method for structural optimization. *Int J Numer Methods Eng* 24:359–373. <https://doi.org/10.1002/nme.1620240207>
- Vatanabe SL, Lippi TN, de Lima CR et al (2016) Topology optimization with manufacturing constraints: a unified projection-based approach. *Adv Eng Softw* 100:97–112. <https://doi.org/10.1016/j.advengsoft.2016.07.002>
- Verbart A, Langelaar M, Van Keulen F (2017) A unified aggregation and relaxation approach for stress-constrained topology optimization. *Struct Multidiscip Optim* 55:663–679. <https://doi.org/10.1007/s00158-016-1524-0>
- Wang Y, Kang Z (2017) Structural shape and topology optimization of cast parts using level set method. *Int J Numer Methods Eng* 111: 1252–1273. <https://doi.org/10.1002/nme.5503>
- Wang F, Lazarov BS, Sigmund O (2011) On projection methods, convergence and robust formulations in topology optimization. *Struct Multidiscip Optim* 43:767–784. <https://doi.org/10.1007/s00158-010-0602-y>
- Wang C, Xu B, Meng Q et al (2020a) Numerical performance of Poisson method for restricting enclosed voids in topology optimization. *Comput Struct* 239:106337. <https://doi.org/10.1016/j.compstruc.2020.106337>
- Wang C, Xu B, Meng Q et al (2020b) Topology optimization of cast parts considering parting surface position. *Adv Eng Softw* 149:102886. <https://doi.org/10.1016/j.advengsoft.2020.102886>
- Xia Q, Shi T, Wang MY, Liu S (2010) A level set based method for the optimization of cast part. *Struct Multidiscip Optim* 41:735–747. <https://doi.org/10.1007/s00158-009-0444-7>
- Xia L, Zhang L, Xia Q, Shi T (2018) Stress-based topology optimization using bi-directional evolutionary structural optimization method. *Comput Methods Appl Mech Eng* 333:356–370. <https://doi.org/10.1016/j.cma.2018.01.035>
- Xie YM, Steven GP (1993) A simple evolutionary procedure for structural optimization. *Comput Struct* 49:885–896. [https://doi.org/10.1016/0045-7949\(93\)90035-C](https://doi.org/10.1016/0045-7949(93)90035-C)
- Xu S, Cai Y, Cheng G (2010) Volume preserving nonlinear density filter based on heaviside functions. *Struct Multidiscip Optim* 41:495–505. <https://doi.org/10.1007/s00158-009-0452-7>
- Yang RJ, Chen CJ (1996) Stress-based topology optimization. *Struct Optim* 12:98–105. <https://doi.org/10.1007/BF01196941>
- Yang D, Liu H, Zhang W, Li S (2018) Stress-constrained topology optimization based on maximum stress measures. *Comput Struct* 198: 23–39. <https://doi.org/10.1016/j.compstruc.2018.01.008>
- Zein I, Huttmacher DW, Tan KC, Teoh SH (2002) Fused deposition modeling of novel scaffold architectures for tissue engineering applications. *Biomaterials* 23:1169–1185. [https://doi.org/10.1016/S0142-9612\(01\)00232-0](https://doi.org/10.1016/S0142-9612(01)00232-0)
- Zhang W, Zhao L, Gao T (2017a) CBS-based topology optimization including design-dependent body loads. *Comput Methods Appl Mech Eng* 322:1–22. <https://doi.org/10.1016/j.cma.2017.04.021>

- Zhang W, Zhao L, Gao T, Cai S (2017b) Topology optimization with closed B-splines and Boolean operations. *Comput Methods Appl Mech Eng* 315:652–670. <https://doi.org/10.1016/j.cma.2016.11.015>
- Zhou L, Zhang W (2019) Topology optimization method with elimination of enclosed voids. *Struct Multidiscip Optim* 60:117–136. <https://doi.org/10.1007/s00158-019-02204-y>
- Zhou M, Fleury R, Shyy Y-K et al (2002) Progress in topology optimization with manufacturing constraints. In: 9th AIAA/ISSMO

Symposium on Multidisciplinary Analysis and Optimization. American Institute of Aeronautics and Astronautics, Reston, Virginia

Publisher's note Springer Nature remains neutral with regard to jurisdictional claims in published maps and institutional affiliations.